December 2017

# Modulation of Photonic Mode Density in Silver Nanodisks and Far Field Focusing of Light by Coupled Plasmonic Nanorings

Longyu Hu
*Clemson University*, longyuh@g.clemson.edu

# Modulation of Photonic Mode Density in Silver Nanodisks and Far Field Focusing of Light by Coupled Plasmonic Nanorings

---

A Dissertation
Presented to
the Graduate School of
Clemson University

---

In Partial Fulfillment
of the Requirements for the Degree
Doctor of Philosophy
Analytical Chemistry

---

by
Longyu Hu
December 2017

---

Accepted by:
Dr. Apparao Rao, Committee Chair
Dr. Ramakrishna Podila
Dr. Jeffrey Anker
Dr. Ya-Ping Sun

# Abstract

During the past twenty years, plasmonic nanostructures have evolved as one of the most promising candidates for applications in miniaturized optical and electronic devices, bio-sensors and photonic circuits, etc. Silver nanoparticles can interact with light more strongly than any known materials with similar dimensions, and support tunable optical properties based on their size, shape and sounding medium, which are more stable than optical properties of traditional pigments and dyes.

Thanks to the recent progress in the synthesis of various silver nanoparticles with different shape and sizes, which has opened doors to the exciting research field of plasmonics. However, silver nanoparticles tend to aggregate when cast on substrates from its aqueous suspension, which compromises their plasmonic properties. In Chapter 2, we describe a simple and reliable method to immobilize silver nanoparticles on polymer coated substrates to mitigate aggregation and allow further chemical modification of silver nanoparticles, if needed. In this project, interesting nanostructured craters were discovered, which were extensively studied using atomic force microscopy (AFM).

Fluorescence is widely used in many biosensing applications such as the quantification of disease markers, protein activity, cytokine and small molecule signals. Metallic nanoparticles alter fluorescence emission by influencing either the incident excitation field, or the radiative and non-radiative decay rates of dye molecules. In Chapter 3, we describe a simple method for tuning the shape of silver nanoparticles to synergistically achieve high fluorescence enhancements in an ensemble of dye molecules. Specifically, we show that the fluorescence emission from Rhodamine B (RhB) is enhanced by >30 folds (with respect to RhB on bare glass) in the presence of Ag nanodisks due to a simultaneous increase in the excitation intensity and photon mode density. Moreover, our detailed finite-element simulations, which account for incident, scattered, and dipole radiated electric fields,

evidenced that the enhancement is strongly dependent on the orientation of RhB dipole relative to Ag NPs and nanodisks.

While aggregation of silver nanoparticles is not desirable, it facilitates creation of fascinating nanostructures that exhibit new properties due to the mystical coupling between plasmonic resonances of particles within the aggregate. Prior research has shown that such coupling leads to Fano resonances, greatly enhanced local electromagnetic fields, unidirectional scattering of light, etc. In Chapter 4, we describe a method for assembling silver nanoparticles into specific configurations, such as a linear chain or a nanoring by manipulating individual silver nanoparticles into such configurations with the help of the AFM tip. We discovered novel far field focusing properties of light by nonorings, which is a result of coupled plasmonic resonances of nanoparticles present within the nanoring.

# Acknowledgments

First and foremost I would like to appreciate my advisor, Prof. Apparao Rao, for saving my Ph.D. career through his continuous support of my study with his great patience, rich fund of knowledge, as well as his network. He is the most helpful and kind advisor I have ever known, and in his research group the students and staff work together and make progress as a family. I was lucky to join his group. My sincere thanks also goes to Prof. Ramakrishna Podila, who gave me many great and useful suggestions. I was very impressed at how practical and applicable Prof. Podila's ideas were. For example, some of the striking dark-field images of the nano-assemblies reported in this thesis originated from his suggestion. I also thank Prof. Jeffrey Anker for his detailed and professional suggestions, and all the support and encouragement from Prof. Ya-Ping Sun. Both of them graciously served as my committee members.

My sincerely thanks to Prof. Georgia Chumanov for providing me access to his state-of-the-art Atomic Force Microscope (AFM), and for training me well in silver nanoparticle synthesis and AFM techniques, as well as for his expertise and useful discussions. I also would like to thank Prof. Joseph Thrasher for introducing me to Clemson University during my interactions with him in Shanghai.

My sincere thanks also goes to Prof. Hai Xiao and his Ph.D. students, Qi Zhang and Jianan Tang for their selfless help with optical measurements. I especially thank Prof. Xiao for the

help and encouragement he rendered when I was in difficulties. Prof. Xiao is not only an outstanding academician but also a brave man with a chivalrous spirit in my opinion. I also appreciate Dr. Wei Liu from Witec In. for all his patient technical support for the near-field optical microscope (NSOM).

My colleagues also gave me a lot of support and help, I especially thank Sai Mallineni for his useful discussion and time, Achyut Raghavendra for his contribution in the simulation work, and Dr. Pradyumna Mulpur for his professional suggestions and interesting conversations about various topics. Thanks to Wren Gregory for her great help and assistance with dark-field microscopy, and it was always fun to work with her. I also thank Yongchang Dong and Fengjiao Liu for their help and caring and I wish them much success, as well as Aubrie Pfirman for her selfless help and her pioneering work with the nano-craters reported in this thesis. I also appreciate Prof. Sriparna Bhattacharya, Anthony Childress and Lakshman Ventrapragada for their valuable advice and assistance. Zhenyu Zhou, Mari L. Emori and Chengqian Luo also provided me great help with statistical analysis. I would like to thank Dr. Andrew Krayev and Dr. Dmitry Evplov from AIST-NT Inc. for their patient technical support which I received during my research at Clemson.

I would like to thank Prof. Shiou-Jyh Hwu for his encouragement in my career pursuits and his contributions in promoting the friendship between the young people from both sides of the Taiwan Straits at Clemson. Special thanks to Dr. Frankie Felder, Ms. Alesia Smith, Ms. Ebony Clemmons, Ms. Kadijah Houston, Dr. Connie Mobley for their outstanding support. Finally, I would like to thank my parents for their love and support, and all my beloved friends who made my life interesting and colorful, Xiang Li, Min Peng, Xinying Wen, Xinxin Zhang, Xin Zhao, Dr. Xiaolin Liu, Dr. Roy Rusly, Dr. Haijun Qian, Aubrie Pfirman, Haodong Li, Ebony Clemmons, Dr. Yiqun Zhang, Ziwen Cheng, Zhe Gao, Yuvaluck Setboonsrung, Dehui Lin, Zhenyu Zhou, Yi Zhang, Yunzhu Luo, Hao Zuo, Xiaotian Liu, Mengyuan Yuan, Mari L. Emori, Xingyu Kang, Jun Peng, and all other friends not mentioned here. And, Ms. Barbara Lewis, I will miss you and your smile.

# Table of Contents

# List of Figures

# Chapter 1

# Introduction to light matter interactions and experiment techniques

Light matter interactions have been studied in several contexts such as, understanding the color of the sky, rainbows, and clouds since prehistoric times; and much of the classical experimental studies were related to the far-field behavior. Although both near and far field descriptions were included in the original classical studies, the former was inaccessible for experimental verification until the advent the nanoscience and nanotechnology. The rapid advances in nanotechnology, and light matter interactions at nanoscale have led to the development of plasmonic materials, viz., materials that exhibit collective oscillations of free electrons. Although, plasmonics effects were known in the literature since early 21$^{st}$ century, it was only after the advent of nanotechnology that the field of light scattering by small particles came into prominence due to its continuing surprising phenomena with new insights and applications. Since then, plasmonic properties of nanoparticles have found its way into a wide range of applications for cancer detection [1], solar cells [2], single molecule fluorescence [3], surface enhanced Raman scattering [4], and super-fast computing chips [5].

Light scattering by small particles is an important problem in electrodynamics, which was first introduced by Lord Rayleigh in 1871 through the concept of an electric dipole moment. A homogeneous electromagnetic field incident on the particle induces a polarization (i.e., the induced dipole), which is determined by the dielectric function of the material (e.g., gold or silver), leading to the scattering of the light. The main assumption is that the phase remains constant over a region of interest since the particle size is less than the wavelength of light.

## 1.1 Lorentz-Drude model

In order to study the optical properties of materials one employs the classical harmonic oscillator formalism as introduced by Lorentz. According to the Lorentz model, the dielectric function of a non-conducting material can be written as

$$\varepsilon = 1 + \frac{f}{\omega_0^2 - \omega^2 - i\gamma\omega} \quad (1.1),$$

where $\omega_0$ and $f$ represent the resonant frequency and oscillator strength of the bound electrons, and $\gamma$ is the damping constant. However, for metals the Lorentz model is modified as the Lorentz-Drude model which takes into account the contribution of free electrons, which is expressed as

$$\varepsilon = 1 - \frac{\omega_p^2}{\omega^2 + i\gamma_e\omega} + \sum_j \frac{f_j}{\omega_j^2 - \omega^2 - i\gamma_j\omega} \quad (1.2),$$

where the summation is over different oscillators. The free electron part in the above equation represents the contribution due to the electron plasma of the metal, which is described by the parameters $\omega_p$ and $\gamma_e$ that represent the resonant plasma frequency and damping constant of bulk plasma. When light is incident on a metallic particle, the charges are set in oscillation where the net effect is manifested in the emission of secondary radiation known as scattering. In addition to scattering, part of the incident radiation may be extinguished within the particle provided that it is absorbing, i.e., having a complex index of refraction. Hence, scattering and absorption leads to the temporal implication of reduction of the incident light after traversing a particle. The net effect of radiation extinguished from the incident beam is termed extinction.

### 1.1.1 Mie theory

Rayleigh scattering describes the elastic scattering of light by spheres that are much smaller than the wavelength of light, and the intensity of the Rayleigh scattered radiation increases

rapidly as the ratio of particle size to wavelength increases. Furthermore, the intensity of Rayleigh scattered radiation is identical in the forward and reverse directions. The Rayleigh scattering model breaks down when the particle size becomes larger than ~10% of the wavelength of the incident radiation. In the case of particles with dimensions greater than this, Mie's scattering model can be used to determine the intensity of the scattered radiation which differs from Rayleigh scattering in several respects: it is roughly independent of wavelength and it is larger in the forward direction than in the reverse direction. The greater the particle size, the more of the light is scattered in the forward direction.

The early studies of light scattering by small particles were developed by Lorenz and Thomson towards the end of the $20^{th}$ century [6]. However, a better understanding of scattering of light from spherical particles was provided by Gustav Mie in 1908 which laid the foundation for light matter interactions. Notably, Mie theory provided a rigorous solution based on electromagnetic theory for scattering of light by spherical particles with sizes that are similar to the wavelength of the light. Mie theory in modified form, also called corrected Mie theory, can be readily used to explain light scattering by particles of non-spherical shape such as ellipsoids or cylinders with an arbitrary radius regardless of the composition of the particles and medium. Importantly, the Mie theory is also applicable to scattering of light by any number of particles even in the absence of coherent phase relations; in other words, when distances between particles are large enough so that there are no coherent phase relations among the scattered light from different particles. An example of a shortcoming of the Mie theory is the electromagnetic hot spot between two nearby particles, which depends on coherency.

A description of light scattering by spherical particles can be obtained by solving the Laplace equation for the scalar electric potential in the quasi-static approximation (refers to equations that keep a static form and do not involve time derivatives even if some quantities are allowed to vary slowly with time),

$$\nabla^2 \Phi = 0 \text{ and } E = -\nabla \Phi \qquad (1.3),$$

with the following boundary conditions

$$\Phi_1|_a = \Phi_2|_a \text{ and } \varepsilon_p \frac{\partial \Phi_1}{\partial r}\bigg|_a = \varepsilon_m \frac{\partial \Phi_2}{\partial r}\bigg|_a \tag{1.4}$$

where $E = E_0\mathbf{z}$, $a$, $\varepsilon_p$ and $\varepsilon_m$ represent the electric field along the $z$ direction, radius of the particle, and the dielectric functions of the particle and the medium, respectively. By comparing the scattering potential from Laplace equation with that of a dipole, the effective dipole moment can be expressed as [7]

$$P = 4\pi\varepsilon_m a^3 \frac{\varepsilon_p - \varepsilon_m}{\varepsilon_p + 2\varepsilon_m} E_0 \tag{1.6}$$

where $P$ represents the dipole moment. The incident electric field on the particle induces a dipole moment, and the scattering field radiated by the dipole can be used to determine the scattering and absorption cross sections. The related expressions for cross sections are as follows [7]:

$$C_{sc} = \sigma_{geom} Q_{sc}, \quad Q_{sc} = \frac{8}{3} q^4 \left| \frac{\varepsilon_d - 1}{\varepsilon_d + 2} \right|^2 \tag{1.7}$$

$$C_{abs} = \sigma_{geom} Q_{abs}, \quad Q_{abs} = 4q \mathrm{Im}\left[ \frac{\varepsilon_d - 1}{\varepsilon_d + 2} \right] \tag{1.8}$$

where $\sigma_{geom} = \pi a^2$ is the geometrical cross section. $Q_{sc}$ and $Q_{abs}$ are dimensionless cross sections of scattering and absorption respectively, and $q = ka$ represents the dimensionless size wherein $k$ is the wave vector of light in the medium. Lastly, $\varepsilon_d = \varepsilon_p/\varepsilon_m$ represent the relative dielectric function. The absorption and scattering cross sections are proportional to particle size as $a^3$ and $a^6$ respectively, which implies that the absorption efficiency will dominate over scattering as the particle size is decreased. Thus, it is difficult to detect very small particles by light scattering.

## 1.2 Materials and Methods

### 1.2.1 Silver nanoparticles

The use of silver metal dates back to the times of Greeks and Romans. Vessels made of silver were used to store water to prevent microbial contamination. In early 1800's silver was used in medical applications, e.g., silver nitrate was used in eye drops and administered to new born babies. In the early 1900's silver was also used to heal wounds. While bulk silver has been used by mankind for centuries in applications ranging from simple ornaments to wound healing, it is only after the advent of nanotechnology and development of advanced characterization techniques that silver nanoparticles found extensive use in advanced fields such as plasmonic solar cells [2], photocatalysis [8], antibacterial coatings for use in washing machines and fabrics [9], conductive inks [10], surface enhanced Raman spectroscopy (SERS) [4], metal enhanced fluorescence [11], biological markers [12], DNA sensors [13] and gas detectors [14].

Moreover, when silver nanoparticles are excited by an electromagnetic radiation, light matter coupling results in strong localized surface plasmon resonances. When an external electro-magnetic field is incident on the metal, the conduction electrons undergo collective oscillations known as plasma oscillations, or plasmons. These plasmons are often confined to the metal surface and are spatially localized in case of nanoparticles (size < 100 nm). This surface plasmon oscillation has an associated resonance frequency which is different from the plasma frequency of the bulk metal. Thus, surface plasmon resonance (SPR) is defined as a collective oscillation mode of plasma localized near the metal surface (LSPR). Of all the metal nanoparticles, Au and Ag nanoparticles (AuNPs and AgNPs) have been extensively studied due to their large scattering cross sections. This dissertation is mainly focused on study of plasmonic properties of AgNPs for the following reasons:

a) AgNPs interacts with light more strongly than any other known materials with the same dimensions;

b) The synthesis of size- and shape-tunable AgNPs has been vastly studied in recent years,

which makes AgNPs ideal materials with optical tenability;

c) AgNPs are chemically stable in both aqueous and air and the cost of silver is much lower than gold as well,

The LSPR oscillation is dependent on the shape and size of the Ag nanoparticles. In general, larger the dimensions of Ag nanoparticles, longer are the resonant wavelengths [7].

### 1.2.2 Synthesis of silver nanoparticles

The AgNPs were prepared by reducing saturated silver oxide solution in ultrapure water using ultrahigh purity hydrogen at 73℃ [15]. By controlling the reaction time and simultaneously monitoring the extinction spectra of the suspension, the size of the Ag NPs can be controlled. The reaction can be represented as

$$Ag_2O(aq) + H_2(g) \longrightarrow 2Ag^0(s) + H_2O(l)$$

The obtained AgNPs were polyhedral single crystals as shown in Figure 1.1 and Figure 1.2 with a narrow size distribution determined from both AFM and TEM studies. AgNPs with varying size distributions were synthesized according to the experimental need.

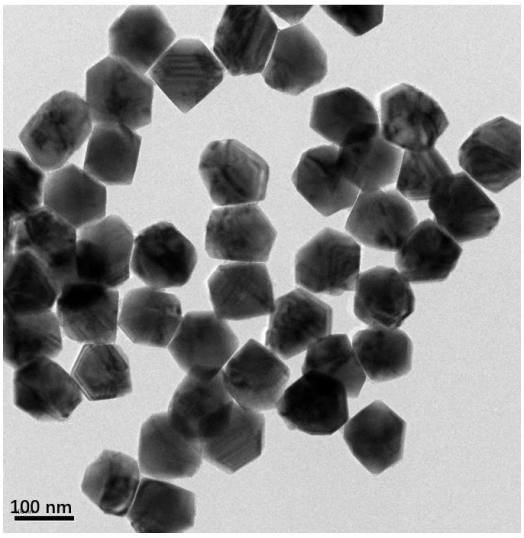


**Figure 1.1** TEM image of as-synthesized AgNPs.

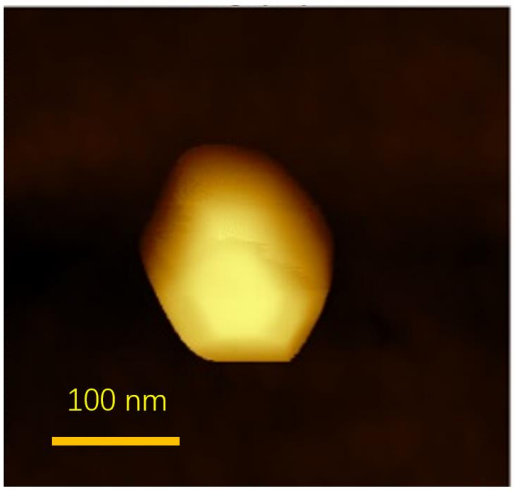


**Figure 1.2** An AFM image of as-synthesized AgNP.

### 1.2.3 Atomic Force Microscopy

The scanning tunneling microscope (STM) was first invented in 1981 by Gerd Binnig and Heinrich Roher at IBM Zürich, which could provide topographic imaging with extremely high resolution (0.1 nm lateral resolution and 0.01 nm depth resolution) for conducting and semiconducting samples. In STM, a conductive tip is brought in very close proximity (~ 0.3-1.0 nm) of the sample surface so that electrons tunnel between the sample surface and the tip via quantum tunneling effect when a voltage bias is applied between them. The resultant tunneling current provides information about the tip-surface distance and the local density of states (LDOS) of the sample. Since STM only works for conducting and semiconducting samples, and a few years later the atomic force microscopy (AFM) was invented which could facilitate topographic imaging of even insulating samples with high resolution.

Typically, an AFM contains these basic components (Figure 1.3): 1) a micron-scale cantilever with a sharp tip (also termed as probe, which is normally made of silicon or silicon nitride) at one end of the cantilever; 2) a scanner made of piezoelectric

materials which controls the X-Y-Z position of the tip on the sample surface; 3) a laser which measures the deflection of the cantilever, and a detector which records the change in the position of the reflected laser beam; and 4) a feedback loop which helps the tip maintain a constant interaction with the sample.

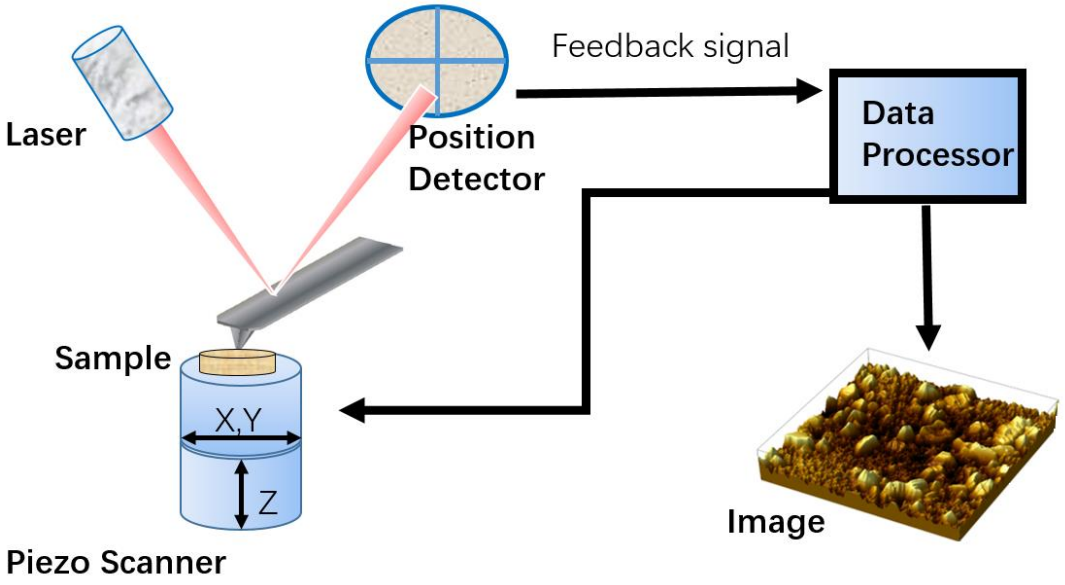


**Figure 1.3:** A schematic for an atomic force microscope.

When the sharp tip scans across a sample surface, the forces developed between them cause the cantilever to bend in accordance to the Hooke's law. Such forces include van der Waals forces, electrostatic forces, capillary forces, chemical bonding, magnetic forces, etc. By monitoring the deflection of the cantilever using the laser-detector combination, the distance between the tip and sample surface can be inferred, and thus a topographic image can be generated by scanning the tip across the sample surface. The first design of AFM in 1986 employed the contact mode, which is typically used for characterizing the topography of hard samples. In the contact mode configuration (Figure 1.4), the cantilever is designed to scan over the sample surface at a fixed deflection which means a constant force is maintained on the cantilever during the scan. Normally the resonant frequency of typical

cantilevers is around 50 KHz and its force constant is below 1 N/m. Contact AFM can measure samples in air, liquids or vacuum. In ambient condition, strong capillary forces exist due to the presence of a thin liquid film on the surface of the sample which decreases the resolution, and this problem can be circumvented by operating the AFM either in vacuum or a liquid. Notwithstanding the above attributes, contact AFM is not suitable for biological samples since they often tend to be soft or weakly bound to the surface and hence could easily be damaged by the AFM tip.

Later in 1987, the non-contact mode of operation was introduced for the AFM, which is capable of scanning even soft samples without causing any damage due to much lower forces exerted on the sample compared to that in the contact mode operation. In the non-contact mode, the AFM tip is excited at its resonance frequency by a piezoelectric transducer, and this oscillating tip senses the van der Waals forces. Normally a constant tip-sample distance is maintained during the non-contact mode operation, and the changes in the amplitude, frequency and phase of the cantilever are recorded. It is worth mentioning that the phase imaging provides image contrast arising from the differences in surface adhesion and viscoelasticity, which is very useful for characterizing co-polymers or distinguishing different components with similar height but different surface chemistry properties.

As mentioned above, by bringing the tip closer to the sample surface under ambient conditions may lead to a liquid meniscus between the tip and sample which is a major problem during contact mode operation. To overcome this issue, the tapping mode operation (also named AC mode, dynamic contact mode, or intermittent contact mode) was developed in 1993, which has become the most widely used AFM mode since it can be used for samples either in air or liquids. In the tapping mode, the oscillating tip at its resonant frequency gently taps the surface of the sample. The stable oscillations of the tapping tip are expected to overcome adhesive and capillary forces which is a significant problem in contact mode. Another advantage of operating AFM in the tapping mode is that

the gentle tapping mitigates the damaging lateral forces compared with those in the non-contact mode.

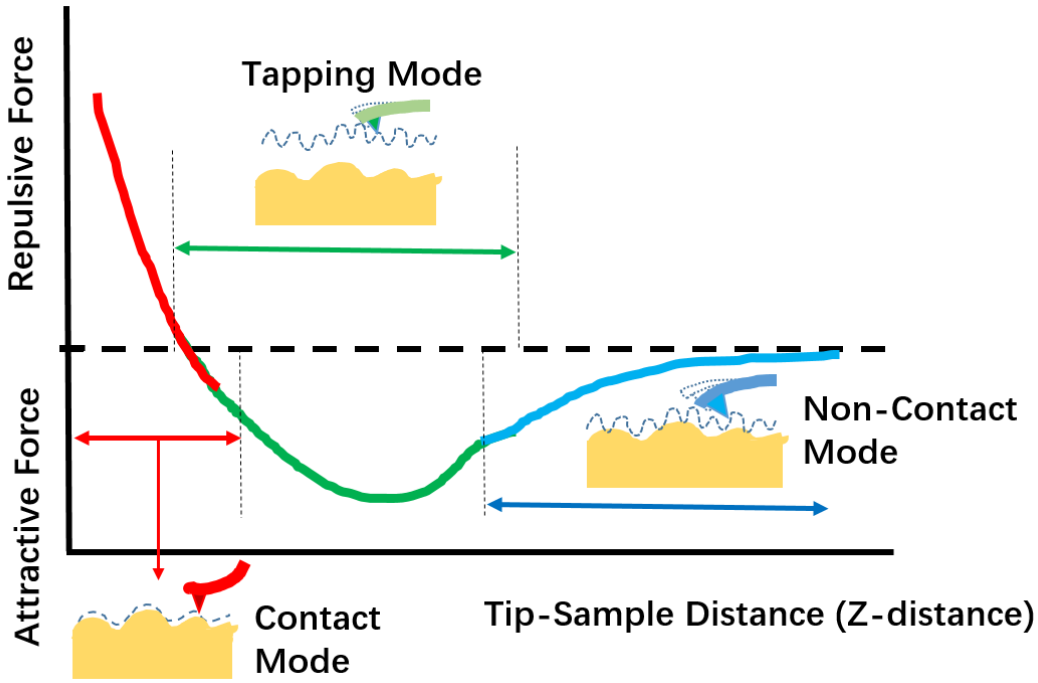


**Figure 1.4** A schematic for the contact, non-contact and tapping mode operations of an AFM.

Other AFM operation modes include the: 1) lateral force microscopy (LFM) where the probe torsional movement is monitored and the frictional forces are measured, 2) conductive AFM where the conductivity map of the surface is measured by monitoring the current flow between the tip and the surface, 3) Kelvin mode which measures the surface potential of the sample, 4) electric force microscopy (EFM) which measures electric field gradient distribution on the sample, and 5) magnetic force microscopy (MFM) which characterizes the magnetic field distribution on a sample. Overall, AFM is a powerful surface technique for not only characterizing sample surfaces with nanoscale resolution but also for elucidating the properties of the sample surface through LFM, EFM and MFM maps without destroying or altering the surface of the sample.

In this dissertation, AFM topographic imaging is used extensively to characterize isolated and arrays of AgNPs.

### 1.2.4 AFM manipulation

Not only can AFM characterize sample surfaces and provide topographic and phase images, but can also manipulate nanoparticles present on a substrate. This goal is achieved by switching the AFM between its contact and tapping mode operations in the following sequence (Figure 1.5): 1) scan a selected area under tapping mode to obtain a clear topographic image, 2) place the AFM tip next to a selected nanoparticle, 3) switch the AFM contact mode to decrease the tip-nanoparticle distance which consequently increases the interaction between tip and the nanoparticle of interest, 4) move the AFM tip, and thus the nanoparticle, to the desired location on the substrate under contact mode (normally the nanoparticle would be pushed by the AFM tip during this step), and 5) switch AFM back to the tapping mode operation and scan the area of interest on the substrate to confirm that the nanoparticle moved to the desired location. By repeating these steps, and with patience and care, complicated configurations of nanostructures can be assemble, which have come to be known as artificial atoms in the field of plasmonics.

In this dissertation, AFM manipulation was used extensively to prepare coupled plasmonic nanoring structures by moving individual naked polygonal silver nanoparticles on glass.

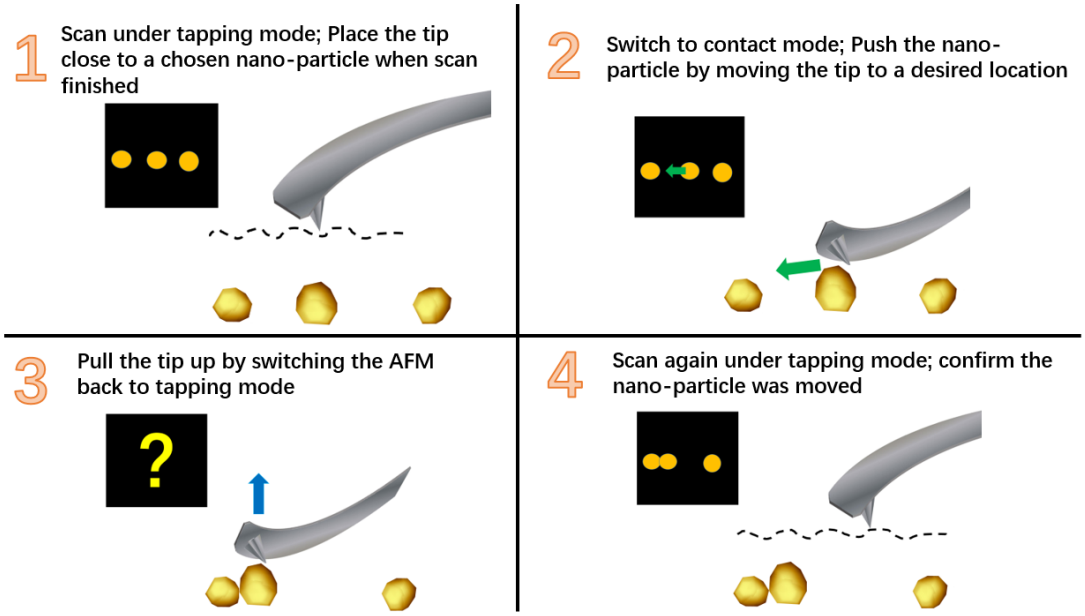


**Figure 1.5** A schematic for the AFM manipulation of nanoparticles.

## 1.3 Transmission electron microscopy (TEM)

In 1873, Ernst Abbe discovered the fundamental resolution limit, which is known as the Abbe diffraction limit and is roughly half the wavelength of light. The wavelength of visible light ranges from about 350-750 nm, which is not suitable for studying nanoparticles by conventional optical microscope. Electromagnetic radiation with shorter wavelength, such as ultraviolet or x-rays, were considered as plausible options as illumination sources in an optical microscope, but the resolution was still insufficient for nanoparticles. The negatively charged electrons possess a mass of 9.1 $\times 10^{-31}$ kg and a de Broglie wavelength that is much shorter than that of visible light, which theoretically provides a much better resolution compared to light. More importantly, electrons are influenced by electric and magnetic field, which provides the possibility of the manipulating and focusing of electron beam as well as imaging. The invention of electrostatic lens and magnetic lens enabled the concept of imaging electron beams after they have interacted with the sample.

A typical TEM consists of: 1) a vacuum chamber which is maintained at a low pressure of $10^{-7}$ to $10^{-9}$ Pa, 2) an electron gun (the illumination source) from which the electrons are emitted upon heating; 3) an electron lens which focuses the parallel electron beam at a focal plane; 4) an aperture, which is a ring-shaped metal plate, which blocks those electrons scattered at large angles and only allow axial electrons to pass. Although a TEM has excellent resolution of 0.1 - 0.2 nm, the disadvantage of the TEM includes the following: 1) measurements must be performed with samples under vacuum; 2) the thickness of the sample must be reduced to submicron scale due to strong scattering and absorption of electrons by the sample; 3) the focused electron beam may heat up the sample and even damage it.

In this dissertation, TEM was used to characterize silver nanoparticles which is an electron dense material, and high quality images with high contrast were obtained.

## 1.4 Dark-field microscope

While the stars are clearly visible at night they can hardly be seen during the day due to the fact that the bright sunshine masks the relatively weaker light from the stars. Compared to a conventional bright-field microscope, a dark-field microscope uses a similar concept and excludes the unscattered light from the image to enhance the contrast and provide high quality images of the sample. In the former, both the illuminating light and the light scattered by the sample are collected, while in the latter, only scattered light is collected by the objective lens and the illuminating light is blocked from reaching the detector. This is realized by a simple design (Figure 1.6) - an opaque disc (termed as a light stop or beam stop) is placed underneath the condenser lens to form a hollow cone of light (in contrast, a full cone of light is used to illuminate the specimen) and the central illumination rays along the optical axis of the microscope are blocked. Only oblique rays with large angles are incident on the sample, and the light scattered from the sample is collected by the objective

lens. In a dark-field microscope, the entire field of view appears dark when no sample is present on the microscope stage.

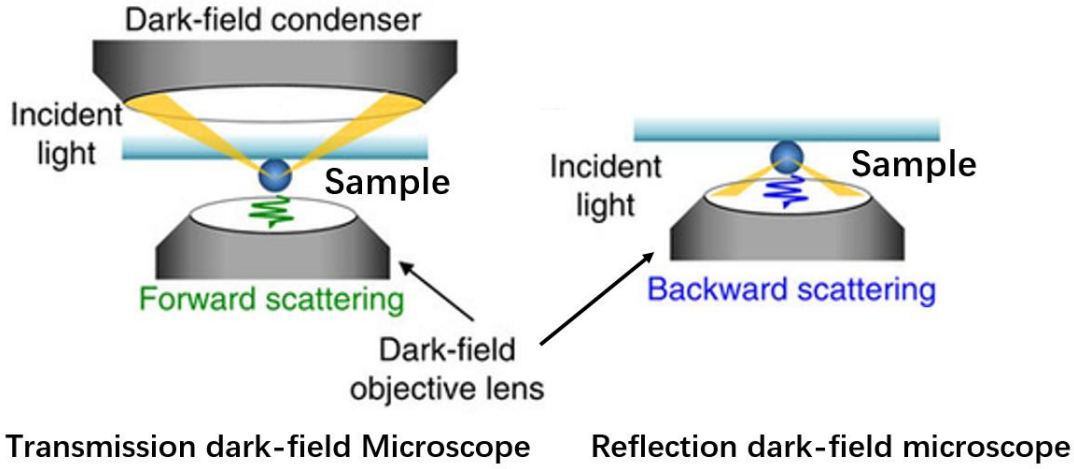


**Figure 1.6** A schematic for a transmission dark-field microscope (left) and reflection dark-field microscope (right). Figure reproduced from reference [16].

In this dissertation, isolated and assemblies of AgNPs were viewed using a dark-field microscope, and high quality images were recorded with excellent signal-to-noise ratio. Moreover, the scattered light spectra revealed exciting plasmonic phenomena which are described in subsequent chapters.

## 1.5 Ultraviolet–visible spectroscopy (UV-Vis)

UV-vis spectroscopy measures the wavelength and intensity of absorption of a sample in the near-ultraviolet and visible spectral range. Typically, as in Figure 1.7 an UV-Vis spectrometer contains of: 1) an illumination source; 2) the monochromator including the entrance slit, a dispersing element which spreads light into various wavelengths, and the exit slit, 3) the sample, and 4) the detector.

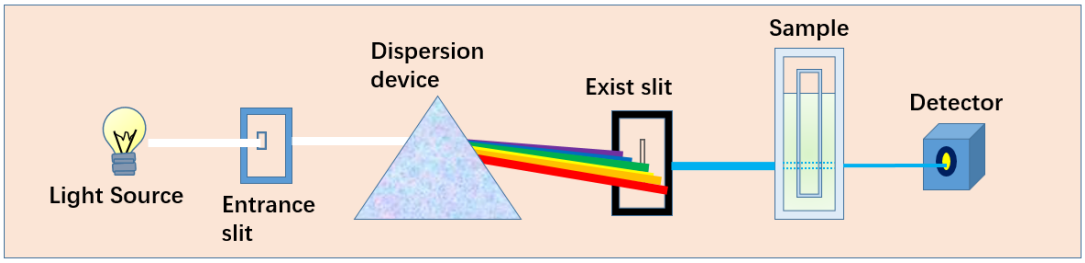


**Figure 1.7** A schematic of a single beam UV-Vis spectrometer.

UV-Vis spectroscopy is widely used to characterize molecules and inorganic ions or complexes in solution. By measuring the absorbance signal at a particular wavelength, the analyte's concentration in the solution can be determined using the Beer-Lambert law since the measured absorbance is proportional to the analyte concentration. This principle can be also be applied to determine the concentration of silver nanoparticles in a colloid suspension at relatively low concentration. The diameter of silver nanoparticles determines its resonance spectrum: 1) according to Mie theory, smaller particles mainly absorb light rather than scatter light; 2) smaller diameter particles experience more uniform electromagnetic field and hence behave more as a dipole due to a strong restoring force with its resonance peak position in the blue region of the electromagnetic spectrum; 3) large particles whose diameters are comparable to the incident wavelength experience relatively less uniform electromagnetic field leading to a quadrupolar behavior, or even higher order modes whose resonance peak position is located in the red region of the electromagnetic spectrum. The UV-Vis spectroscopy can be also used to monitor the particle size during their synthesis and also serve as a quick way to estimate aggregation of AgNPs in a suspension.

In this dissertation, UV-Vis spectroscopy was used to measure the resonance peak of 2D arrays of AgNPs, AuNPs and $Ag_2S$ NPs.

# Chapter 2

# Stabilization of 2D assemblies of silver nanoparticles by spin-coating polymers

## 2.1 General Introduction

Silver nanoparticles (AgNPs) self-assembled on poly(4-vinylpyridine) modified surfaces were spin-coated with poly(methyl methacrylate), poly(butyl methacrylate) and polystyrene from anisole and toluene solutions. The polymers filled the space between the particles thereby providing stabilization of the assemblies against particle aggregation when dried or chemically modified. The polymers did not coat the top surface of the nanoparticles rendering chemical accessibility to the AgNP surface, which was confirmed by converting stabilized AgNPs into silver sulfide through electrochemical reduction of AuNPs. Etching away the AgNPs resulted in crater-like polymeric structures extending down to the underlying substrate. This study has been published in Applied Surface Science, Volume 357, p. 1587-1592.

## 2.2 Background

When AgNPs are closely spaced, the coupling between the collective electrons oscillations (the plasmon coupling) in individual particles results in new plasmon modes. It was previously demonstrated that the coherent plasmon coupling in 2D arrays of self-assembled AgNPs produces a sharp resonance that can be used for various sensing applications owing to its sensitivity to the refractive index of the surrounding medium [17,18]. In addition, the enhanced local EM field in spaces between the nanoparticles was utilized for surface enhanced Raman spectroscopy [19]. The plasmon coupling depends on the interparticle

distance, particle size and the dielectric constant of the surrounding medium. As the dielectric constant increases, or the interparticle distance decreases until the optimum value, the coupling becomes stronger for the same size of the particles [20,21]. However, even a small degree of aggregation has a detrimental effect on the coherent coupling and the sharpness of the resonance peak.

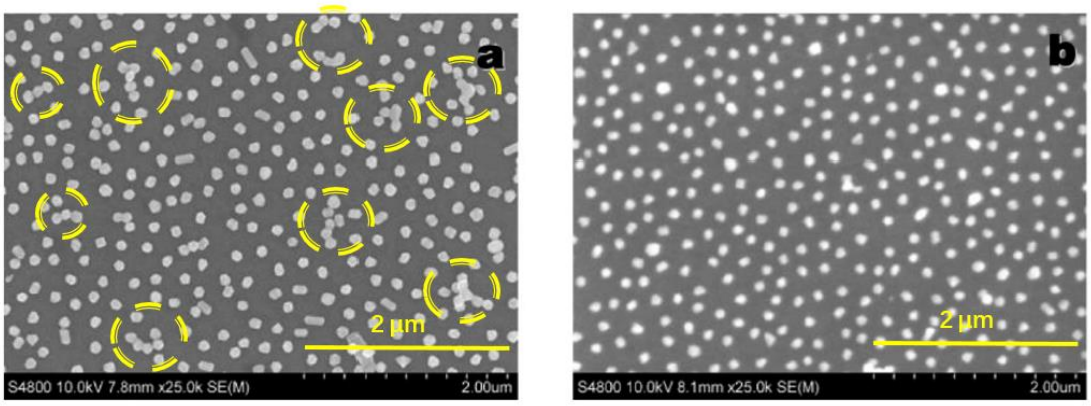


**Figure 2.1** SEM images of dried AgNP arrays on a bare substrate (left) and a substrate treated with 5% PMMA solution (right). The circled regions in the left image show the aggregated AgNPs. Figure reproduced from reference [21].

The self-assembly of nanoparticles is an efficient and easily scalable method for fabricating nanostructured surfaces. It is often challenging to maintain such assemblies without particle aggregating on the surface, particularly when there is a need for further chemical modifications or the transfer of the assemblies into different media. For example, drying 2D assemblies of AgNPs causes the nanoparticles to aggregate into clusters due to the solvent surface tension producing lateral forces on the particles as in Figure 2.1 [22]. Consequently, solvents with lower surface tension, from which the self-assembly is carried out, tend to cause less aggregation when drying. It is important to recognize that particles aggregate even when they are chemically attached to the surface that is uniformly modified with affinity ligands as in the case of metal nanoparticles on thiolated surfaces. However, when the affinity ligands are patterned on the surface, the aggregation of nanoparticles is

less critical because the particles are physically confined to only patterned areas [22–24]. The aggregation is usually an irreversible process, and the particles remain aggregated after rewetting the assemblies. This causes irreproducibility or complete loss of properties of nanostructured surfaces [22].

Malynych et al. stabilized the coupled 2D array of Ag NPs and preserved their sharp plasmon resonance by embedding the arrays into a poly(dimethylsiloxane) matrix. However the particles were fully covered by the polymer coating which rendered the metal surface unsuitable for chemical modifications [22]. Matrubara et al. reported the fabrication of silver nanodisks on both flat and textured surfaces by transfer-printing, and the resulting nanostructures were stable toward aggregation because they were physically anchored to the substrates [26]. In another work, periodic metal nanodot arrays were fabricated by the pulsed laser melting induced fragmentation of prepatterned metal nanostrips [27]. Chichkov et al. reported the use of a laser-induced transfer of molten metal nanodroplets for building 2D and 3D arrays [28]. The nanostructures in both reports were stable because the nanoparticles were spatially confined. The problem of the nanoparticle aggregation in solutions was mainly addressed through chemical modifications of the particles' surface or by encapsulating the particles in protective shells. Negatively charged citrate ions that adsorb on the metal surface stabilize the nanoparticles by the electrostatic repulsion, but such suspensions are limited to low concentrations and the particles aggregate irreversibly upon the addition of electrolytes [29,30]. Thiol groups have high affinity to noble metal surfaces and alkanethiols were used to obtain thermally stable and air-stable metal nanoparticle powders that can be repeatedly re-dissolved in organic solvents [31,32]. Amine, phosphine and its oxide, carboxylate, iodine, isocynide and acetone were also used as stabilizing ligands [33–40]. These small ligands can desorb easily or be replaced by other ligands with stronger affinity to the metal surface.

Nanoparticles coated with a shell of different materials become sterically stabilized and more resistant to high electrolyte con-centration. Poly(4-vinylpyridine) (PVP) stabilized

AgNPs are more stable than citrate stabilized Ag NPs in standard media [41,42]. Polyethylene glycol (PEG) is an inert, amphiphilic and biocompatible linear polymer soluble in water, organic polar and apolar solvents, which forms random coils on the metal nanoparticles' surface when hydrated in water and the particles are stable in electrolytes and biological environments [43–45]. Chitosan is a biodegradable and biocompatible linear polysaccharide used to stabilize noble metal nanoparticles [46,47]. Dendrimers provide both electrostatic and steric stabilization for nanoparticles, so do polymers that form linear chain structures grafted to the nanoparticles' surface [48–50]. Various silica coated metal nanoparticles were made based on Stöber process usually with controlled thickness by adjusting tetraethyl or thosilicate (TEOS) concentration [51–54]. However, these methods are not very effective for preventing the aggregation of nanoparticles attached to substrates because the particles remain 'free' to roll on the surface. Rubinstein et al. reported metal nanoparticle films on glass stabilized by 3.0–3.5 nm silica coating that preserved the original plasmon response [55].

In this chapter, a simple and reliable method for stabilizing 2D assemblies of AgNPs is described. The method is based on affixing the nanoparticles to substrates with a PVP layer followed by spin-coating polymers in the space between the nanoparticles. Similar method was previously used to change the dielectric function of the medium to study its effect on the plasmon coupling [20,21]. By adjusting the spin-coating parameters, the thickness of the polymer layer can be adjusted to stabilize the assemblies without coating the metal surface. After etching the nanoparticles, crater-like polymeric structures were obtained. A similar approach was used to produce thin porous silicate films with submicron polystyrene spheres as templates as well as silica films on glassy carbon electrodes with 2D assemblies of hemispherical cavities [56,57].

## 2.3 Experiment and results

### 2.3.1. Materials

Hydrogen peroxide (30–35%) from Fisher Science, sulfuric acid (98%) from J.T.Baker, anisole (>99.0%) from Fluka Analytical, ethanol (99.98%) from Pharmco-Aaper, silver(I) oxide (99.99%) powder and hydrogen tetrachloroaurate(III) (99.99%) from Alfa Aesar, ferric nitrate nonahydrate (98.7%) from Fisher Chemical, poly(4-vinylpyridine) (PVP) [MW 60,000], poly(methylmethacrylate) (PMMA) [MW 996,000], poly(butylmethacrylate) (PBMA) [MW 337,000] and polystyrene (PS) [MW 280,000], sodium sulfide nonahydrate (98%) from Sigma Aldrich were used as received. Ultrapure water (<18 MΩ cm) was obtained from Millipore-Q system and both ultrahigh purity nitrogen and hydrogen were purchased from Air Gas. Microscope glass slides (VWR) and ITO glass with $R_s$ = 8–12 Ω/sq. (Delta Technologies) were cut into 25 mm × 15 mm × 1.0 mm pieces. About 120 nm thick Ag and Au films were deposited via the thermal evaporation in vacuum.

### 2.3.2. Instrumentation

UV-2501PC Spectrophotometer (Shimadzu) was used to record UV–Vis spectra. High-resolution TEM-H9500 (Hitachi) was used to characterize the AgNPs (Figure 1.1). All glass and ITO substrates were cleaned with the Plasma Sterilizer PDC-32G (Harrick). AFM measurements were performed in a non-contact mode using AIST-NT SPM Smart system and cantilevers (HQ:NSC14/Al BS-50) from Micromasch. AIST-NT image analysis and processing (Version 3.2.14) software was used for AFM images analysis. Electrochemical Workstation, Model 400 A, (CH Instruments) was used for the electrochemical studies.

### 2.3.3. Synthesis of Ag NPs

The AgNPs were synthesized by reducing saturated silver oxide solution in ultrapure water by ultrahigh purity hydrogen at 73 ℃ in a round bottom flask, as previously reported [15]. The size of the AgNPs can be adjusted by controlling the reaction time simultaneously

monitoring the extinction spectra of the reaction suspension. Colloidal suspensions containing 55 ± 3 nm, 100 ± 5 nm and 120 ± 7 nm AgNPs were used in the study.

### 2.3.4. 2D assemblies of AgNPs

Glass substrates (25 mm × 15 mm × 1.0 mm) were treated by a mixture of 35% hydrogen peroxide and 98% sulfuric acid for 4 h, washed with copious amount DI water, dried with pure nitrogen and cleaned with plasma. Clean substrates were rolled on a hot-dog style roller in 0.01% PVP ethanol solution for 4.5 h, and rinsed several times with ethanol followed by the final rinse with DI water. The PVP modified substrates were exposed at constant agitation to AgNP suspensions (OD = 0.1, 0.3) for different times ranging from 2.5 to 13 h followed by rinsing with water to obtain 2D assemblies with different nanoparticle density as in Figure 2.2.

### 2.3.5. Polymer spin-coating and etching of Ag NPs

The 2D assemblies of AgNPs were immersed first in pure anisole for a few seconds to remove excess surface water followed by immersing into polymer anisole solutions (0.6% PMMA, 1% PMMA, 1.2% PMMA, 1.8% PMMA, 3% PMMA; 1% PBMA; 1% PS, 2% PS, 3% PS) for 2 min. The wet substrates were mounted on a spin coater and additional 30 μL of the corresponding polymer solution was dropped onto the substrates followed by spinning at 5000 rpm for 45 s. The substrates were annealed at 140 ℃ for 10 min. Etching of AgNPs was performed by dropping 45 μL of 1.5 M $Fe(NO_3)_3$ aqueous solution onto the substrates followed by thorough rinsing with DI water after a few seconds of the exposure. The procedures are schematically presented in Figure 1.

### 2.3.6 Electrochemical silver deposition into craters

PMMA-based craters were formed on ITO, Au or Ag coated substrates. Mixture of 0.1 M $Na_2SO_4$ and 0.1 mM $Ag_2SO_4$ deoxygenated by bubbling nitrogen gas for at least 15 min was used as electrolyte in all electrochemical experiments. The metal deposition was

carried out in the ‘bulk electrolysis with coulometry’ mode at potentials between −0.57 V and −0.75 V vs. SHE for 3–10 s depending upon the desired metal thickness.

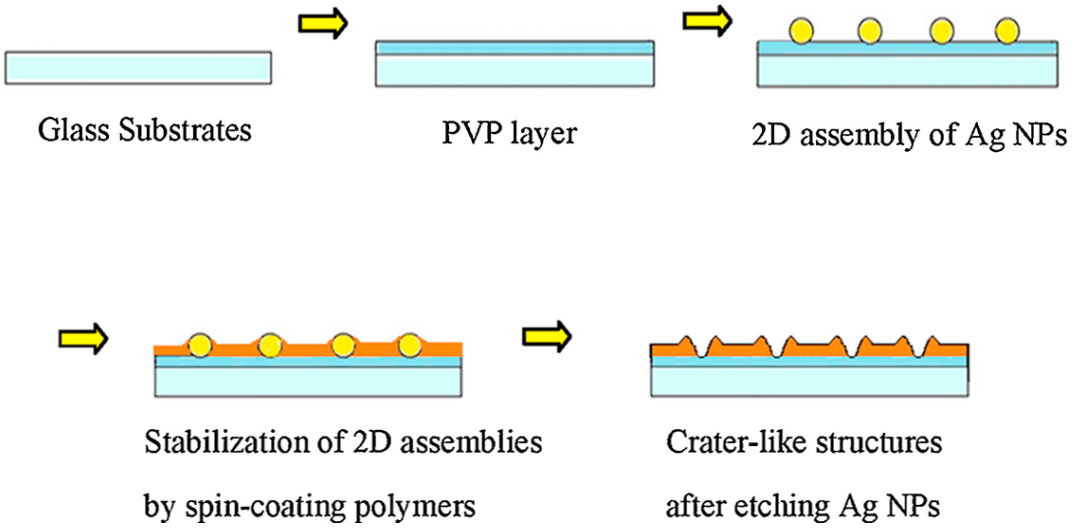


**Figure 2.2** A schematic of general steps of stabilization of 2D assemblies of 2D assemblies by spin-coating polymers

Unmodified microscope substrates made of float glass have an average roughness less than 5 nm. The average roughness was uniformly increased to about 8–9 nm after the PVP modification carried out from 0.01% ethanol solution for 4 h. The roughness was further increased when higher PVP concentrations were used. It is well recognized that high polymer concentrations favor more coiled structures of polymer molecules on surfaces leading to larger roughness [45]. The exposure of the modified substrates to aqueous 100 nm AgNPs suspensions resulted in the 2D self-assembly of AgNPs. The density of the particles on the surface was controlled by adjusting the particle concentration in the suspension as well as the exposure time. The self-assembly was carried out from DI water with low ionic strength providing long range electrostatic repulsion between the particles due to the electric double layer associated with the metal surface. The electrostatic

repulsion kept the individual particles well separated in the assembly. The Ag NPs absorb on the PVP surface through the formation of bonds between the lone pair electrons on the pyridyl ring and the silver surface. Despite this strong interaction, the particles can move on the surface. In order to move a particle to another location, the bond between the particle and the surface needs to be broken; however, a new identical bond is formed at the new location. This movement can be viewed as breaking of existing and simultaneous forming new surface bonds, the process that does not require additional energy. The particle assemblies in water are stabilized by the electrostatic repulsion, but drying negates this repulsion as well as produces lateral forces that push the particles together resulting in the aggregation. The lateral forces are caused by the surface tension of drying water. The stabilization of the particles in the assemblies was achieved by filling the spaces between the particles with polymers. The stabilized assembly could withstand repeated drying/rewetting cycles as well as various chemical modifications while retaining their original arrangement. The method can be applied to other polymer/nanoparticle assembly combinations.

The average height of AgNPs in the assemblies, as measured with the AFM, was $97 \pm 4$ nm (Figure 2.3). The particles appeared with sharp corners suggesting that their surface was not covered with the PVP (Figure 1.2). It was initially suspected that, because of the high affinity of PVP to silver, the polymer molecules adsorbed on the surface of the substrate can also partially cover the particle surface to establish an equilibrium distribution between the two surfaces.

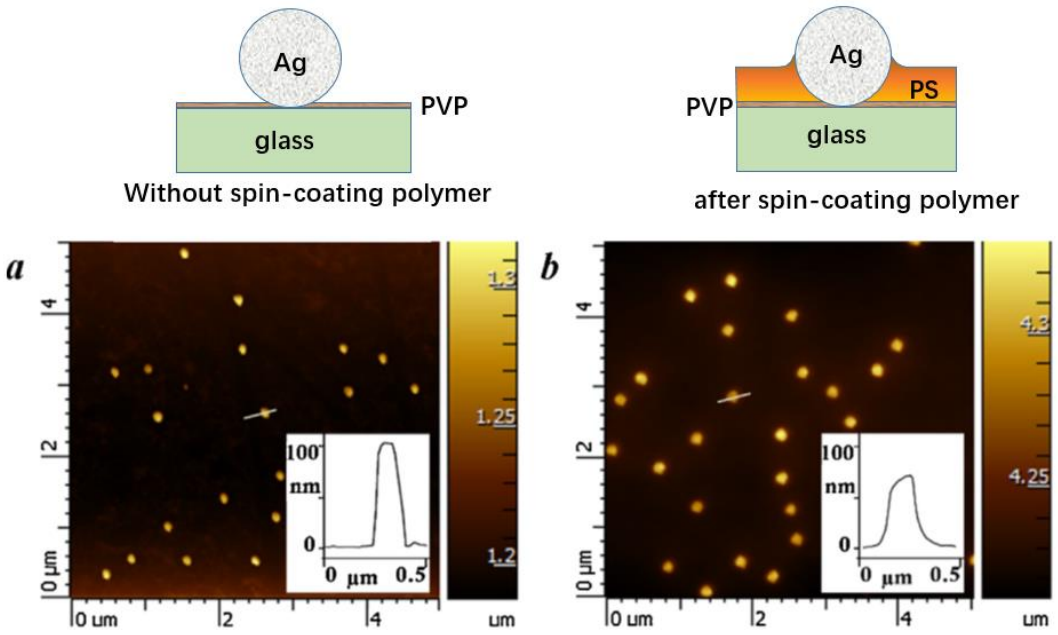


**Figure 2.3** AFM images of 100 nm AgNPs on PVP coated glass substrates: (a) before polymer spin-coating; (b) after spin-coating PS from anisole solution. Insets: height profiles of AgNPs.

To prevent the particle aggregation, the 2D assemblies were stabilized by spin-coating various concentrations of polymers such as PS, PMMA, PBMA from two different solvents, toluene and anisole. After the spin-coating, the average height of the particles decreased depending upon the concentration of the polymer, a general trend observed for all polymers and solvents used in this work. For example, when the PS concentration was increased from 0.3% to 1% and 3%, the average height of Ag NPs decreased from 97 ±3 nm to 90 ±3 nm and 16 ±3 nm, respectively. Further height decrease on the order of a few nm was observed after the substrates coated with 1% PS or 1% PMMA were annealed at 150 ℃ for 25 min. The measured decrease of the particles' height after the annealing seems counterintuitive. One would expect an increase of the measured height because the annealing at temperatures larger than that of the glass transition (~110 ℃) of PS and PMMA will cause the relaxation of the polymers causing the particles to float to the surface

of the polymer layer as neither PS nor PMMA have strong affinity to silver. The relaxation of the polymer layer was concluded from the AFM measurements of the surface roughness that changed from 4–5 nm to 1–2 nm for 1% polystyrene film and from 7–8 nm to 1–2 nm for 1% PMMA film. The discrepancy can be explained by considering the underlying PVP layer that will also soften at this temperature and pull the particles deeper inside the layers due to the PVPs strong affinity to silver. Mixing of PVP layer with PS or PMMA layers is also possible at this temperature.

When the 2D assemblies of Ag NPs are stabilized by the spin-coating of polymers, it is important to know whether or not the metal surface is coated with the polymer. To address this question, etching of nanoparticles as well as chemical modifications of the metal surface was undertaken. Ferric nitrate can etch silver because its standard reduction potential (0.77 V) is close to that of Ag+ (0.80 V) and the resultant silver nitrate is a soluble compound [59]. After the etching of the assemblies with molar excess of ferric nitrate crater-like structures were observed thereby indicating that the silver surface was not covered with the polymers or, at least, the polymer layers were not sufficiently dense to prevent chemical accessibility to the metal surface (Figure 2.4). The height and the external diameter of the craters, as measured relative to the area of the substrate containing no nanoparticles, depended on both the type and the concentration of the polymer. For example, 100 nm Ag NPs and 1% of PBMA, PS and PMMA yielded the average height of $40 \pm 3$ nm, $52 \pm 3$ nm, and $50 \pm 4$ nm whereas external diameters were 440–550 nm, and 180–310 nm, 280–350 nm, respectively. No significant differences of the crater structures were found for glass and ITO substrates under the same conditions. Although the crater depth measurements were not reliable due to the limited penetration of the AFM tip inside the craters, there was a noticeable trend in that higher concentrations of polymers resulted in deeper craters. The solvent, in which the polymers were dissolved prior to spin-coating, had also effect on the crater dimensions, e.g. 1% PS in anisole consistently gave taller

craters than 1% PS in toluene [60]. Proportionally smaller craters were observed when smaller Ag NPs were used as templates.

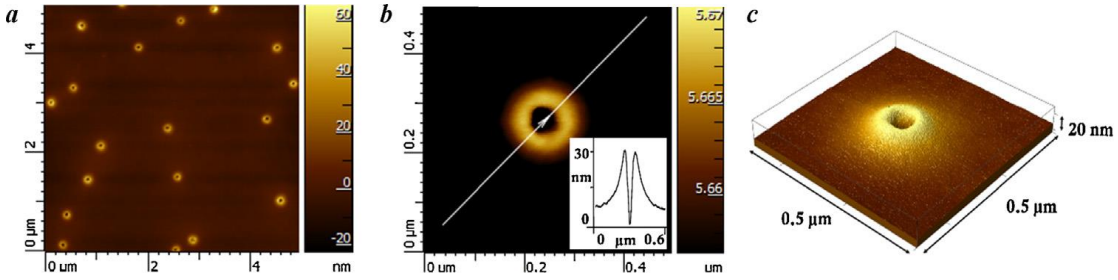


**Figure 2.4** AFM images of crater-like structures after etching AgNPs with $Fe(NO_3)_3$ Inset: the height profile of a crater in (b).

Whereas the dependence of crater dimensions upon the concentration of polymers is rather clear, the dependence upon the type of the polymer, substrate and solvent most likely reflected how the polymer solutions wetted both the substrate and the nanoparticles. The underlying layer of PVP on the substrate is expected to be wetted well by both solvents because of π–π interactions between the aromatic rings. Neither of the polymers nor solvents is expected to have specific affinity to the silver surface, so it is likely that all solutions wetted the surface of the nanoparticles to the same degree. The formation of the craters was due to the capillary force that pulled up the polymer solutions at the particle substrate interface. In the absence of strong interactions between a surface and a liquid, the capillary force depends upon the ratio of the surface tension to solvent density and is larger for anisole polymer solutions thereby leading to consistently larger craters formed from anisole than those from toluene. The dissolved polymers did not change substantially the surface tension from that of the pure solvents as was tested using the drop size method for 1% polymer solutions. In this method, drops of the same volume of different polymers solutions were deposited on clean glass substrates and the spot sizes were compared to that of pure solvents. No statistically meaningful differences of the spot sizes were noticed

thereby concluding that the polymers at such low concentration did not affect the surface tension of the solvents.

Polymer stabilized 2D assemblies of AgNPs were exposed to $HAuCl_4$ aqueous solution with the expectation that the gold salt will etch silver away producing gold nanoparticle (AuNP) assemblies. Indeed, the AFM imaging revealed the presence of nearly spherical particle clusters protruding on average 119 ± 5 nm from the surface of the substrates and arranged in the same way as the original AgNPs (Figure 2.5). Each cluster was composed of roughly 5 smaller gold particles with the estimated size of 30 nm. The UV–Vis spectroscopy confirmed the presence of the plasmon resonance peak at about 547 nm corresponding to small AuNPs as well as a weak shoulder at 645 nm due to the plasmon coupling between the particles in the clusters (Figure 2.5). It was concluded that each AgNP was completely dissolved because the strong plasmonic features from the AgNPs disappeared from the UV–Vis spectra after etching with the gold salt.

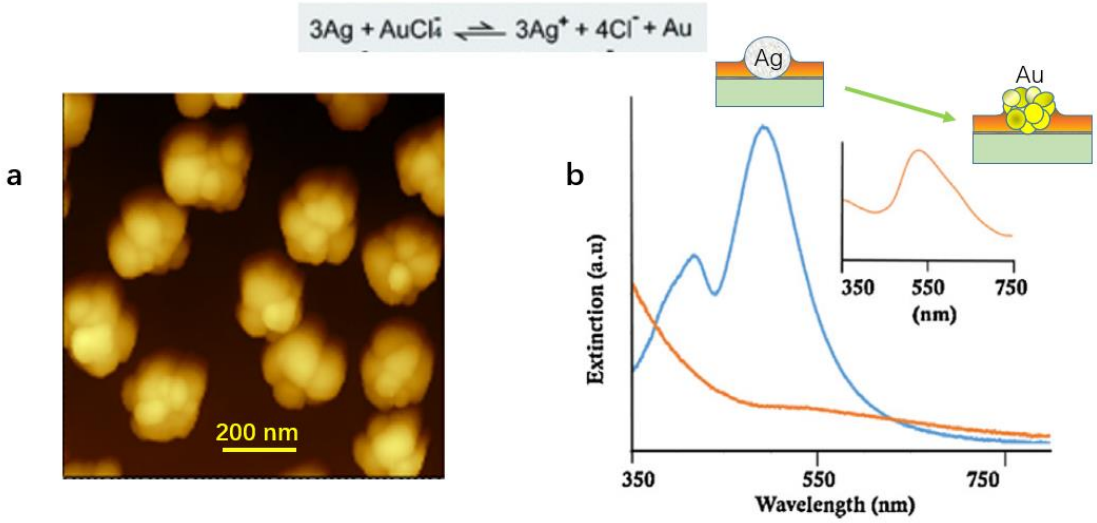


**Figure 2.5** (a) AFM images of Au clusters obtained by $HAuCl_4$ treatment of 120 nm Ag NPs; (b) UV–Vis spectra of 2D assembly before (blue curve) and after (orange curves) the treatment.

The structure of the gold clusters depended upon the surface density of AgNPs on the substrate. The size of the gold clusters was smaller and they appeared more like open circles on the rim of the crates as the AgNPs density decreased. This observation was rationalized as interplay between the local concentration of the zero valence gold and its diffusion from the substrate. Low surface densities of AgNPs lead to low local concentrations of the zero valence gold near the substrate. This zero valence gold partially diffused away from the substrate before it had a chance to assemble into small nanoparticles that became attached to the rim of the craters. At high silver densities, more zero valance gold was available near craters producing more Au NPs that formed 3D gold clusters on top of the craters. The zero valance gold that diffused from the substrate most likely formed AuNPs in the solution; however it was impossible to detect them using UV–Vis spectroscopy to due to their low concentration.

The polymer stabilized 2D assemblies of AgNPs was also treated with $Na_2S$ aqueous solutions. AFM images revealed the simultaneous presence of small nanoparticle clusters and empty craters on the substrates (Figure 2.6).

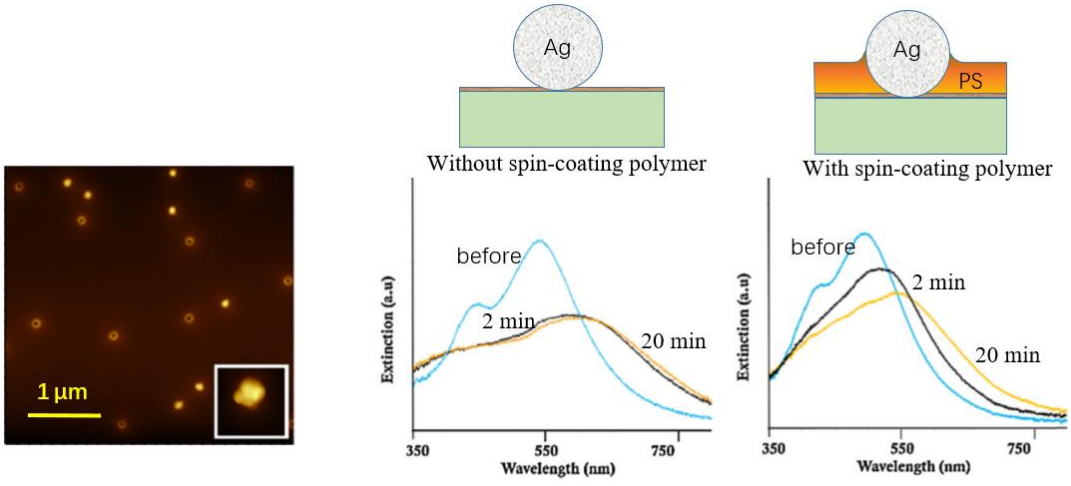


**Figure 2.6** 1% PS after treatment with 0.16 M $Na_2S$ for 3 min. Inset: close-up image of one particle; 0.11 M $Na_2S$ for 2 min (black); 20 min (orange).

The average measured height of the clusters was $94 \pm 5$ nm. The plasmon resonance broadened and shifted to the red spectral region due to the formation of silver sulfide on the surface of the NPs (Figure 2.6). Silver sulfide has a large dielectric function and absorption coefficient casing the red shift and damping of the resonance. The formation of silver sulfide on AgNPs appeared to be a self-limiting reaction as large changes in the UV–Vis spectra were observed during the first minute after exposure to $Na_2S$ followed by only small changes with time. As expected, the rate of the silver sulfide formation in the case of 2D assemblies without spin-coating polymer layer was slightly larger (Figure 2.6). The fact that the 2D assemblies of AgNPs treated with $Na_2S$ retained their plasmonic spectral features, albeit damped, suggested that the nanoparticles composed of a silver core coated with small silver sulfide particles, as was evident from close-up AFM images of individual nanoparticles (Figure 2.6, Inset). The empty craters that were also observed most likely appeared after rinsing the substrates exposed to $Na_2S$ with water. Silver sulfide coated nanoparticles are expected to have no/low affinity to PVP modified substrates and can be easily washed away.

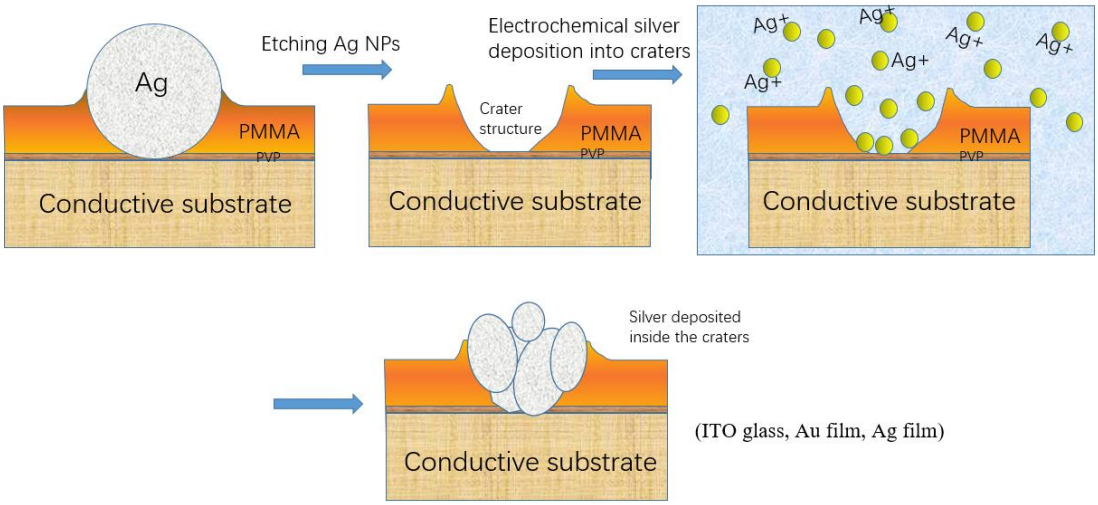


**Figure 2.7** A schematic for electrochemically depositing AgNPs inside the nano-craters.

Attempts were also made to electrochemically grow metallic silver in the craters. ITO, vacuum deposited gold or silver conducting substrates were coated with PVP followed by attaching AgNPs, spin-coating of PMMA and etching the nanoparticles to produce craters (Figure 2.7). The substrates containing craters were connected to the electrochemical workstation and the silver reduction was carried out at −0.58 V and −0.71 V vs. SHE. The growth of silver was not uniform on all three substrates with the gold substrates exhibited the most consistent results (Figure 2.8). AFM imaging revealed craters filled with silver together with empty craters as well as the presence of various size clusters of small AgNPs in the vicinity of the craters (Figure 2.8). The nonuniform electrochemical growth of silver was most likely due to the heterogeneity of the underlying conducting substrates. It is well known, for example, that the electrochemical deposition of metals on bare ITO proceeds via seeded growth, in which the metal reduction begins at defect sites, often at the boundaries between individual ITO crystallites that provide the smallest reduction overpotential [61]. Silver reduction occurred in places where a crater overlapped with such defect site. In some instances, zero silver diffused from the inside of craters forming silver clusters on the outside. More negative reduction potentials resulted in the formation of

larger silver particles/clusters and decreased the number of empty craters.

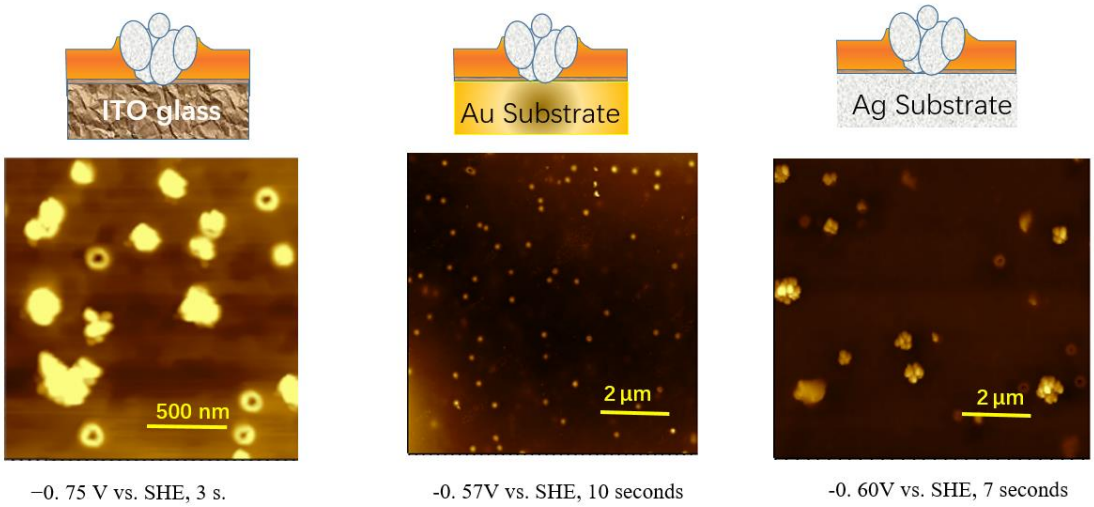


**Figure 2.8** AFM images of AgNPs electrochemically deposited inside the nano-craters on conductive substrates

## 2.4 Conclusions

Spin-coating of polymers onto 2D assemblies of AgNPs was used to stabilize the assemblies against aggregation. The polymer filled the space between the particles leaving the metal surface uncoated and accessible to various chemical reactions. Etching nanoparticles produced crater-like structures, the size of which can be manipulated by changing the polymer concentration and the solvent. The method can be extended to other polymers and nanoparticle assemblies.

# Chapter 3

# Enhancing emission of RhB by tuning the shape of silver nanoparticles

## 3.1 General Introduction

Fluorescence is widely used in many biosensing applications such as the quantification of disease markers, protein activity, cytokine and small molecule signals [62–72]. Accordingly, concerted efforts have been devoted towards achieving strong enhancements in fluorescence for improving the detection sensitivity of biomarkers [68, 72, 73]. The strong light-matter interactions in metallic nanostructures have been used for providing large fluorescence emission intensity enhancements, raise quantum yield, and also tune the far field angular distribution of fluorescence. For instance, silver and gold nanoparticles (Ag and Au NPs) have been widely used for improving the limits of detection through surface plasmon resonance (SPR) and surface plasmon coupled emission (SPCE) [74–76]. Metallic NPs alter fluorescence emission by influencing: A) the incident excitation field, and B) the radiative and non-radiative decay rates of dye molecules [77]. In the case of single-molecule fluorescence [77], these competing effects (A and B) have been experimentally shown to result in either fluorescence enhancement or quenching depending on the separation distance between dye molecules and NPs.

## 3.2 Experiment and results

Here, we posit that NP shape can be tuned to synergistically combine effects A and B to achieve high fluorescence enhancements in an ensemble of dye molecules. Specifically, we show that the fluorescence emission from Rhodamine B (RhB) is enhanced by >30

folds (with respect to RhB on bare glass) in the presence of Ag nanodisks due to a simultaneous increase in the excitation intensity and photon mode density. On the other hand, the fluorescence emission from RhB on polyhedral Ag NPs was at least ~2 times weaker compared to RhB on Ag nanodisks. Our detailed finite-element simulations, which account for incident, scattered, and dipole radiated electric fields, evidenced that the enhancement is strongly dependent on the orientation of RhB dipole relative to Ag NPs and nanodisks. The observed increase in Ag nanodisks is explained in terms of its upshifted scattering closer to RhB emission, which results in an increased local electric field and higher photonic mode density for Ag nanodisks.

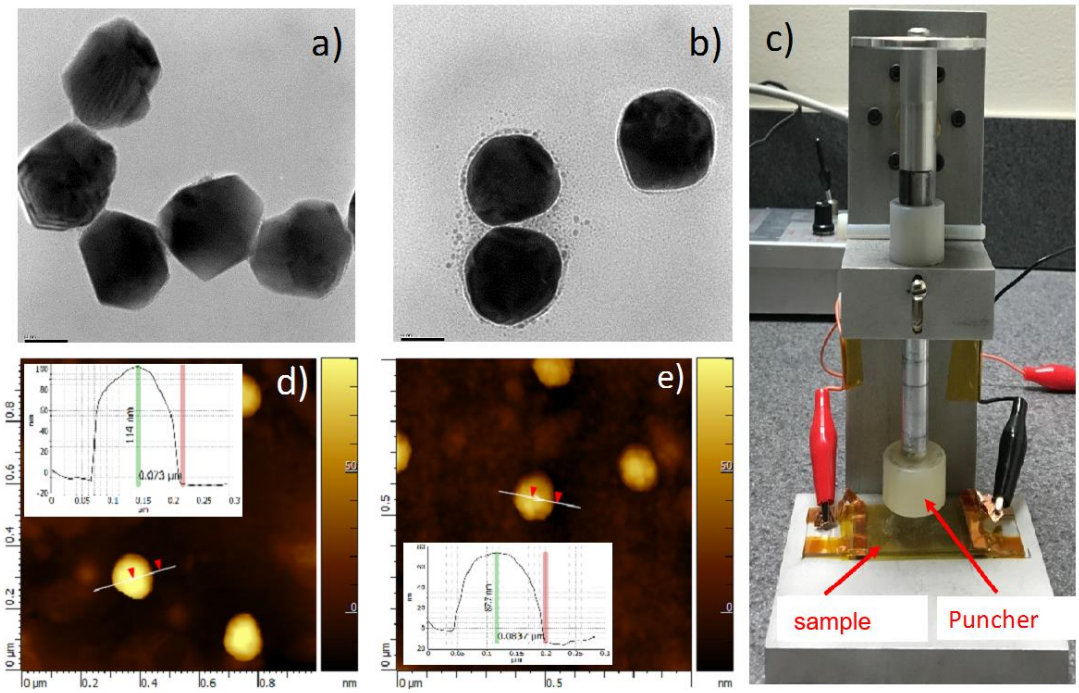


**Figure 3.1** (a) and (b) show TEM images of (a) *unpunched* and (b) *punched* AgNPs (scale bar: 50 nm). A home-built puncher with a Teflon mandrel (c). Zoomed-in AFM images of (d) *unpunched* AgNPs and (e) *punched* AgNPs (@50N/50times) exhibiting a circular shape with reduced height.

For evaluating the effects of nanostructure morphology on RhB emission, polyhedral AgNPs were prepared via the method described in Chapter 2 [15]. Briefly, a saturated aqueous $Ag_2O$ solution was reduced by infusing hydrogen (ultrahigh purity) at ~73 ℃ until a faint yellow color was observed indicating the formation of colloidal AgNPs. The as prepared AgNPs were found to exhibit a polyhedral single crystal morphology having corners, as shown in Figure 3.1a. To prepare AgNP coated slides, bare glass-microscope-slides (25 mm × 15 mm × 1 mm) were functionalized with a polyvinyl pyrrolidone (PVP) layer (~10 nm) by submerging them in a 0.01 wt. % PVP-ethanol solution for 4 hours. Following rinsing and drying, PVP functionalized slides were immersed into the synthesized AgNPs suspension under constant agitation for ~10 hours. This step facilitated the chemisorption of AgNPs that form bonds with the lone-pair electrons on the pyridyl ring of PVP coated on the slides. For altering the NP morphology, the glass-slides coated with AgNPs were deformed through the application of a transverse mechanical force using a home-built, motorized, Teflon coated circular puncher (automated to deliver 50 N force at 2 Hz) with a radius of ~1 cm (see Figure 3.1b inset). As the force was applied only over a part of the slide (corresponding to the puncher area ~3.14 $cm^2$), we were able to obtain both as prepared AgNPs (in the *unpunched* regions) and Ag nanodisks (*punched* regions) on the same glass slide. The as prepared AgNPs were found to be mechanically deformed to nanodisks upon subjecting them to a force of 50 N for 50 times (Figure 3.1b). Although AgNPs displayed different morphologies before and after mechanical deformation, the lateral size of unpunched (104.5 ± 10 nm) and punched NPs (112.5 ± 9 nm) gleaned from transmission electron microscopy (TEM) was similar, with the deformed particles exhibiting slightly larger diameters. Considering that TEM is more reliable for measuring the lateral size, we conducted atomic force microscopy (AFM) to understand the effects of applied force on NP height. The unpunched AgNPs showed an average height of ~110 nm which is very similar to their lateral size (~104.5 nm) suggesting that they are nearly

spherical with an aspect ratio (diameter/height) ~0.95 (Figure 3.1c). On the other hand, punched AgNPs exhibited a smooth circular boundary with a height ~88 nm lower than their lateral size (112.5 ± 9 nm) indicative of a more 'disc' shaped morphology with an increased aspect ratio of ~1.34. In a recent publication, AgNPs were also mechanically deformed by rolling process, and at much lower rate (100-1000 micron/second) and resulted in more flattened and elongated nanodisc.

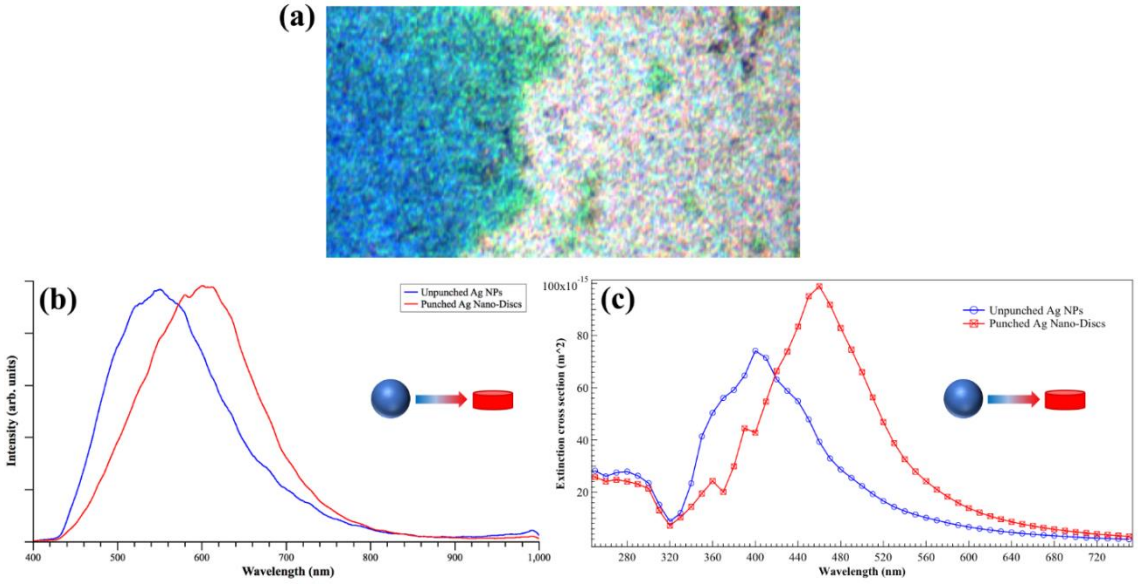


**Figure 3.2** a) A dark field image showing *unpunched* (blue) and *punched* (red) regions of the glass substrate; (b) corresponding red-shifted scattering spectra acquired from Cytoviva optical microscope; and (c) COMSOL simulations showing red-shift in extinction spectra from spherical AgNPs to *punched* Ag nanodisks.

A dark-field transmission optical microscope equipped with the CytoViva hyperspectral imaging system (CytoViva HSI, Auburn, AL) was employed to obtain high-resolution scattering spectra from AgNPs and nanodisks. It is well known that any change in the size

or shape of metallic NPs drastically alters their optical and plasmonic properties [78]. Figure 3.2a shows a dark-field image of the substrate containing both unpunched (i.e., as prepared) and punched AgNPs. While the blue-region represents the unpunched portion of AgNPs, the reddish tinge arises due to the presence of punched Ag nanodisks. The corresponding scattering spectra (Figure 3.2b) showed a clear red-shift from as synthesized spherical AgNPs (~530 nm with a width ~150 nm) to the deformed Ag nanodisks (~600 nm with a width ~180 nm), which is attributed to the increased aspect ratio. To better understand the effects of mechanical deformation, we simulated the extinction spectrum of Ag NPs and nanodisks (with the observed experimental sizes) by numerically solving the Helmholtz wave equation for the total electric field in the full field formulation with a plane wave incidence using COMSOL Multiphysics finite element method (Figure 3.2c). Permittivity values for silver were adopted from Johnson and Christy's work [79]. The simulations confirmed that the higher aspect ratio of Ag nanodisks changes the frequency dependence of the scattered E-field leading to an upshifted peak in their extinction spectrum.

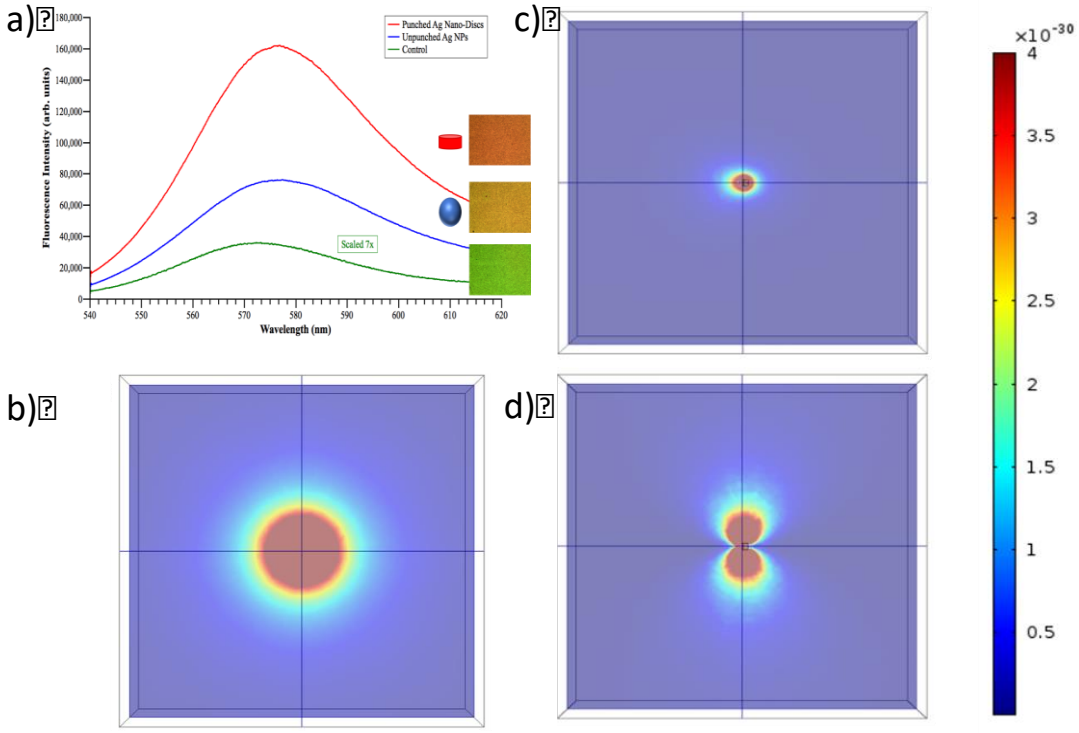


**Figure 3.3** a) A plot showing the comparison of RhB fluorescence intensities recorded from regions consisting of punched and un-punched AgNPs and control substrates (scaled x7 for clarity). Corresponding white-light Raman microscope images are in the inset. (b) COMSOL simulation showing time-averaged Poynting vector for a point dipole located at the center. In the presence of *punched* Ag nanodisks, a dipole positioned at a distance of 10 nm perpendicular (c) or parallel (d) to the nanodisk showed a change in the radiated field symmetry.

The effect of nanoparticle morphology on fluorescence emission was studied by uniformly spin coating (3000 rpm for 60 s to form a ~30 nm overcoat) RhB fluorophore (1 mM) polymethyl methacrylate or PMMA on glass slides containing both punched and unpunched AgNPs. The fluorescence spectra of RhB molecules were collected using a Renishaw inVia micro-Raman spectrometer with a 532 nm laser excitation. Figure 3.3 shows a comparison between the intensity of RhB fluorescence signals produced from

*unpunched* (AgNPs) and *punched* (Ag nanodisks) regions of the substrate. The emission from RhB coated on plain glass-slides served as a *control*. While the *unpunched* AgNPs produced high signal enhancements (~15 fold) over *control* substrates, the fluorescence signal doubled (~33 fold with respect to *control*) for RhB coated on *punched* Ag nanodisks. This result was also reflected in white-light microscope photographs (Figure 3.3 inset), where a more-intense orange color of RhB emission was observed from the Ag nanodisks relative to unpunched AgNPs. The higher enhancements observed for Ag nanodisks may be rationalized through the following analysis.

In a simplified NP-dye model, the presence of NPs in the vicinity of dyes is known to change the frequency $(w)$ dependent radiation field $\vec{E}_{inc}(\omega)$ due to the addition of scattered field ($\vec{E}_{sca}(\omega)$) leading to a new excitation field given by $\vec{E}_{exc}(\omega) = \vec{E}_{inc}(\omega) + \vec{E}_{sca}(\omega)$. While this simplification is apt for some cases such as the single-molecule case, the true excitation field must include an additional secondary field ($\vec{E}_{\text{sec}}(\omega)$) arising from the spontaneous emission of the dye. Each dye molecule acts as an emitting dipole whose field interacts with the NP to in turn backscatter $\vec{E}_{\text{sec}}(\omega)$ as a part of the excitation field. Beyond the single-molecule fluorescence case [16], the backscattered $\vec{E}_{\text{sec}}(\omega)$ may play more significant role in an ensemble of dyes due to a higher number of dye molecules associated with each NP. Thus, the true total excitation field ($\vec{E}_{total}$) for dye ensemble is given by $\vec{E}_{total}(\omega) = \vec{E}_{exc}(\omega) + \vec{E}_{\text{sec}}(\omega)$. Based on Maxwell's equations, the secondary field may be expressed as $\vec{E}_{\text{sec}}(\omega) = \vec{\vec{G}}(r,r',\omega).p(\omega)$, where $\vec{\vec{G}}(r,r',\omega)$ is the dyadic Green's function connecting the *E*-field at a position *r* due to a dipole at *r*' while $\vec{p}(\omega)$ is the dipole moment of RhB [73, 79, 80, 81]. Thus, a self-consistent expression for the frequency-dependent dipole moment may be obtained from

$$\vec{p}(\omega) = \alpha(\omega)\vec{E}_{total}(\omega) = \alpha(\omega)\left(\vec{E}_{exc} + \vec{E}_{\sec}\right) = \alpha(\omega)\vec{E}_{exc} + \alpha(\omega)\vec{\vec{G}}(r,r',\omega).\vec{p}(\omega) \qquad (3.1),$$

where $a(w)$ is the polarizability of the dye. Considering the dipole moment to be aligned along a direction $\hat{e}_d$ yields the magnitude of $p(w)$ given by

$$p(\omega) = \frac{\alpha(\omega)\left(\hat{e}_d \bullet \vec{E}_{exc}\right)}{1 - \alpha(\omega)\left(\hat{e}_d \bullet \vec{\vec{G}}(r,r',\omega) \bullet \hat{e}_d\right)} \quad . \qquad (3.2),$$

If the backscattered field from the radiating dipoles is ignored then the second term in the denominator becomes zero resulting in the standard form of the dipole moment. As mentioned earlier, the presence of NPs influences the excitation (effect A) due to changes in the local field. The NP-induced excitation enhancement is proportional to the ratio of square of the local electric field with and without NPs. Given that $\vec{p}(\omega) = \alpha(\omega)\vec{E}_{total}(\omega)$, the excitation enhancement factor (*EEF*) is equivalent to the ratio of square of the dipole moment strengths in the presence/absence of the NP.

$$EEF = \left(\frac{\hat{e}_d \bullet \vec{E}_{exc}}{\hat{e}_d \bullet \vec{E}_{inc}}\right)^2 \frac{1}{\left(1 - \alpha(\omega)\left(\hat{e}_d \bullet \vec{\vec{G}}(r,r',\omega) \bullet \hat{e}_d\right)\right)^2} \quad . \qquad (3.3),$$

While the traditional excitation enhancement occurs solely due to the scattered field, the above expression for *EEF* combines the effects of secondary field dependent on an extra "field term" $\left(\hat{e}_d \bullet \vec{\vec{G}}(r,r',\omega) \bullet \hat{e}_d\right)$ related to the dipole field. Similar to the enhancement of

excitement intensity, the presence of NPs also alters the radiative decay rate (effect B). The radiative decay rate ($\gamma$) of a dye molecule, from an excited state $|k\rangle$ of energy $E_k$ to a lower state $|n\rangle$ of energy $E_n$, through the emission of a photon of energy $\hbar\omega$ may be understood in terms of the Fermi golden rule given by

$$\gamma = \frac{2\pi}{\hbar}\sum_{n\neq k}\left|\langle n|\vec{p}\bullet\vec{E}_{tot}|k\rangle\right|^2\delta\left(E_k - E_n - \hbar\omega\right) \quad . \qquad (3.4),$$

The Fermi golden rule can also be expressed in terms of photon mode density or $r(r,w)$ within the vicinity of the dye, which is defined as the ratio of photon flow per unit area per second (i.e., power flow per photon) to the velocity of photons

$$\gamma = \frac{2\omega}{3\hbar\varepsilon_o}\langle p\rangle^2\rho(r,\omega) \qquad , \qquad (3.5),$$

where, $\rho(r,\omega) = \frac{6\omega}{\pi c^2}\left(\hat{e}_d\bullet\vec{\vec{G}}(r,r,\omega)\bullet\hat{e}_d\right)$.

The photon mode density, and thus the decay rate of a dye, is determined by the field term $\left(\hat{e}_d\bullet\vec{\vec{G}}(r,r',\omega)\bullet\hat{e}_d\right)$ containing the dyadic Green's function of the system in which the dye is embedded. The field term $\left(\hat{e}_d\bullet\vec{\vec{G}}(r,r',\omega)\bullet\hat{e}_d\right)$ is frequency dependent and is sensitive to the changes in the scattering spectrum of the surrounding NPs. Given that the punched AgNPs or nanodisks show a red-shift in their scattering (closer to the emission of RhB), it may be rationalized that the field term at the emission frequency of RhB is higher for Ag nanodisks compared to polyhedral AgNPs due to increased local field from scattering. This increase in the field term is expected to simultaneously enhance both the excitation intensity (equation 3.3) and the decay rate (equation 3.5) leading to a higher enhancement.

We validated the observed enhancements by simulating the emission of an electric dipole (mimicking RhB molecule with dipole moment 9.78 D) 10 nm above spherical and punched Ag NP surface using the RF module in COMSOL Multiphysics v5.1. This full field model, which includes the effects of scattered and secondary fields, was used to compute both normalized electric field (*normE*) and time-average Poynting vector ($P_{av}$) (see Figures 3.3 b-d). Our simulations evidenced that the electric field of the radiating dipole changed from a spherically symmetric shape to a dumbbell shape in the presence of both AgNPs and nanodisks. Furthermore, the simulations showed that the total enhancement factor is dependent on the orientation of the dipole. The dipole showed a higher enhancement when it is oriented parallel to the NPs. Our experiment randomly averages the orientation of RhB in the dye ensemble relative to AgNPs or nanodisks. Thus, we obtained the overall enhancement factor from simulations by weighing 2/3 parallel versus 1/3 perpendicular direction. The $P_{av}$ for Ag nanodisks showed a higher enhancement factor ~10 times over free space and ~4 times relative AgNPs concurring with our experimental results.

## 3.3 Conclusion

In summary, we experimentally found that the NP-induced enhancement in RhB fluorescence emission can be increased up to ~33 folds by tuning the NP morphology. We produced Ag nanodisks through mechanical deformation of polyhedral AgNPs dispersed on a glass slide. The higher enhancement factors in the presence of Ag nanodisks (~33 fold) compared to AgNPs (~15 folds) are rationalized in terms of the higher contribution from secondary *E*-field comprised of dipole radiation scattered by the nanostructure. The Ag nanodisks exhibited an upshift in their scattering spectrum due to a higher aspect ratio with a peak (~600 nm) closer to the RhB emission (~580 nm). Such an upshift resulted in a

better enhancement of both excitement intensity and radiative decay rate of RhB in the presence of Ag nanodiks relative to AgNPs. The experimentally observed upshift in scattering and the higher enhancement factors for Ag nanodisks were validated by a COMSOL finite element model, which considered the effects of both incident and scattered electric fields.

# Chapter 4

# Far-field Focusing of Visible Light by Coupled Plasmonic Nanorings

In this work, far-field light focusing of visible light was achieved by coupled plasmonic nanorings, which were prepared by AFM manipulation of ~110 nm diameter AgNPs. The relationship between the focal length and nanoring dimension was systematically studied. For a better understanding of the plasmonic coupling within the nanoring structures, the resonance scattering spectra of various nanoring structures were measured in the transmission mode using dark-field microscopy. Nano-crescents also showed similar light focusing as the full nanorings do. This result is interesting and highly useful in manipulating visible light in both near-field and far-field.

## 4.1 General Introduction

### Instruments

The Atomic force microscope (AFM) topographic imaging and the AFM manipulations were performed using a AIST-NT SPM Smart system. AFM probes (HQ:NSC14/Al BS-50) used for both AFM topographic imaging and AFM manipulations were purchased from Micromasch. AIST-NT image analysis and processing (Version 3.3.105ex1) software was used for AFM topographic analysis. As described in Chapter 1, the AFM manipulation of AgNPs into nanorings was achieved by switching the AFM between its contact mode and non-contact mode of operation.

The optical images of the plasmonic nanorings were collected by a 100x objective (UPlan Fl, 1.3NA) in a WITec Alpha 300S system under reflection mode. The WITec Alpha 300S system enabled fine control (~20 nm for each step) for moving the nanorings in and out of the focal plane. A home-made microscope system with a 100x objective (UPlan Fl, oil immersion, 1.3NA) was also used to view the nanoring structures under transmission mode. A Mira-900 laser (Coherent Inc.) was used to create laser-etched marks (width of 5 microns) on the coverslip substrates on which the nanorings were prepared. These marks were used for locating specific nanorings when the coverslip was transferred back-and-forth between the AFM and the dark field microscope. Transmission dark-field images and forward scattering resonance spectrum were collected by the CytoViva widefield hyperspectral imaging system; and reflection dark-field images were collected by a custom built WITec Alpha system.

## 4.2 Preparation of coupled plasmonic nanorings by AFM manipulation

### 4.2.1 Laser etched marking of coverslips

Since manipulation of AgNPs using an AFM tip happens on a nanometer scale (which is far below the resolution ability of human eye) and the fact that AFM can only scan a limited area (normally hundreds or thousands of micon$^2$), it is vital for the user to be able to quickly locate a specific nanostructures on the substrate (which in this study happens to be a coverslip) during AFM manipulation. Otherwise, it can be extremely challenging to systematically manipulate individual AgNPs into nanorings and spectroscopically characterize them.

Coverslips (thickness of 0.17 mm) were first cleaned with acetone and followed with rinsing with DI water and air drying. Next, a Mira-900 laser (Coherent Inc.) was used to etch micron scale marks at the center of the coverslips which were easily visible under an

optical microscope. Normally, the width of the laser etched marks is between 4-8 microns, and asymmetric Roman letters such as “D” “F” are preferred since they can help in easy determination of the location of the nanorings on the coverslips, and help distinguish the top and bottom sides of the coverslip. Some hieroglyphic is also a good option for laser etched marking for their asymmetric shape. Figure 4.1 illustrates two optical images of etched marks examples of 1) Roman letter “A” “D” and 2) a hieroglyphic beneath the AFM cantilever.

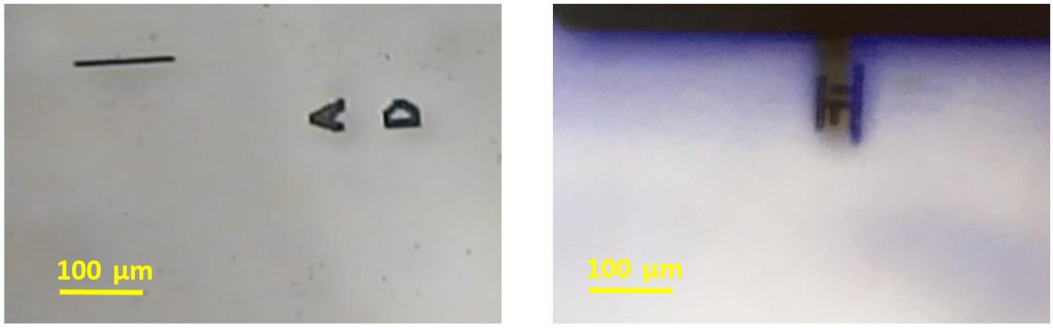


**Figure 4.1** Optical images of laser etched marks on a coverslip. Examples include the Roman letters “A” and “D” (left) and a Chinses hieroglyphic (symbolizing “justice”) located beneath the AFM cantilever (right).

Although these etched marks are tens of microns in dimension (much larger than the nanorings) they appear as tiny white dots on the coverslip to the naked eye and serve as a reliable coordinate for the user to locate nanorings of interest for spectroscopy or imaging.

### 4.2.2 Assembling nanorings of AgNPs via AFM manipulation

The marked coverslips are immersed in aqua regia for ~30 minutes and thoroughly rinsed with DI water, followed by drying with compressed nitrogen or air. Due to the surface tension of water, the AgNPs tend to aggregate during the drying step. To mitigate such

undesirable aggregation, about 50%-90% of ethanol is added to the aqueous suspension to accelerate the drying process. Using a pipette, a single drop (20-30 μL) of AgNP containing water/ethanol suspension is drop cast in the vicinity of the laser etched marking on the coverslip. It is preferred that the casted drop is not spread since a denser distribution of individual AgNPs is more favorable for AFM manipulation as several individual AgNPs will be closer to each other.

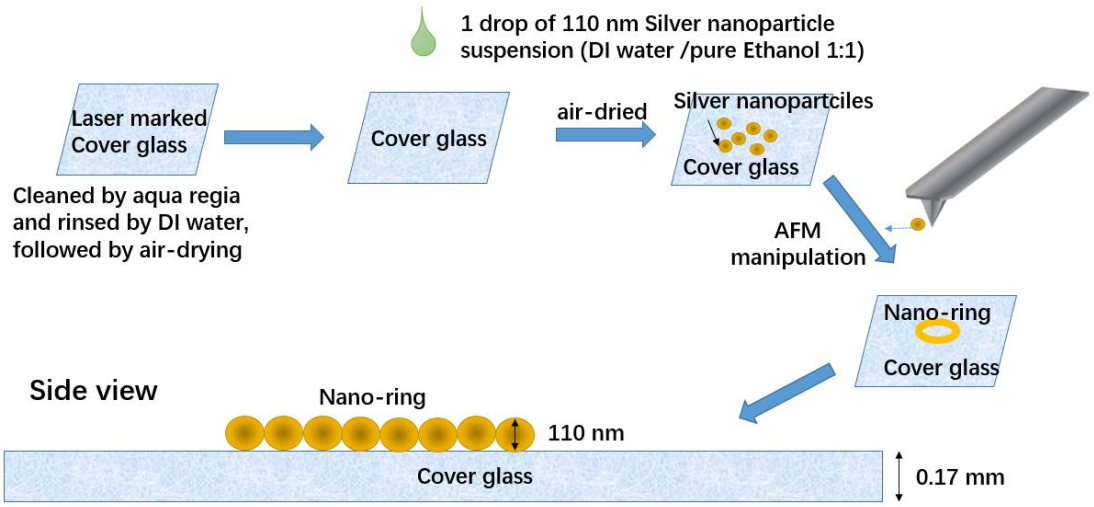


**Figure 4.2** A schematic for assembling coupled plasmonic nanorings via AFM manipulation.

As described in detail in Chapter 1, manipulation of single AgNPs using AFM was achieved via a stepwise process in which the AFM was switched to operate in its contact or tapping modes (semi-contact mode). Several nanorings comprising of naked polygonal AgNPs were created in which each AgNP touches neighboring AgNPs. In all, a trimer and four nanorings consisting of 8, 9, 16 and 24 AgNPs, as well as two incomplete nanorings of 8, 12 AgNPs were constructed for far-field light focusing studies (Figure 4.3). These nanorings were used in light focusing experiments in a dark-field microscope operating in the reflection mode. Another set of nanorings consisting of 8, 11, 12, 16 and 27 AgNPs

were constructed for experiments in a dark-field microscope operating in the transmission. Compared to light focusing data obtained in the reflection mode, much better resolution and improved signal-to-ratio in the light scattering data were obtained in the transmission mode.

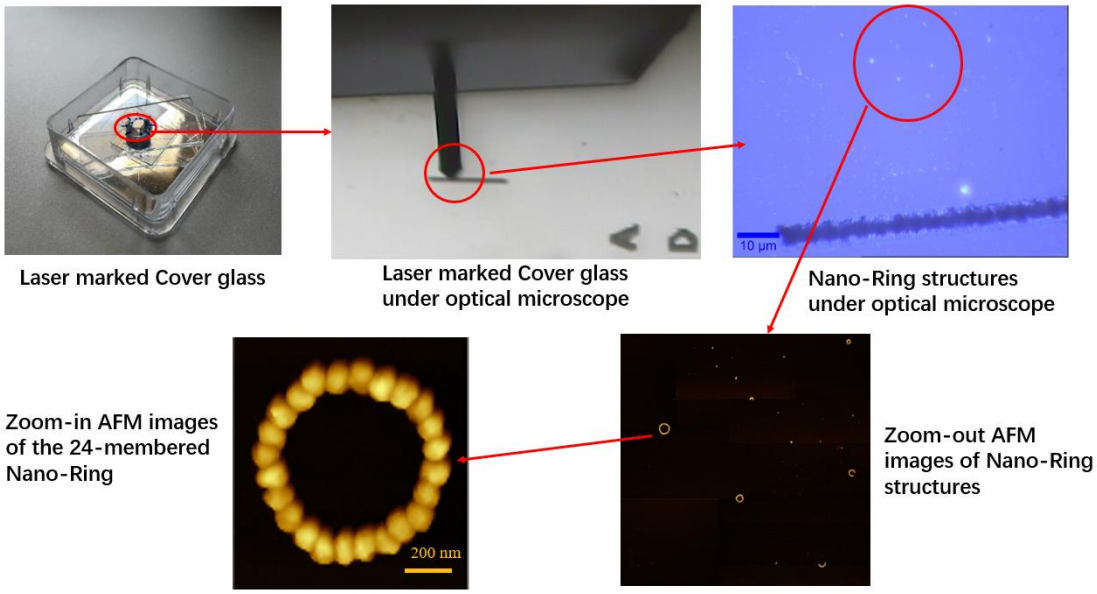


**Figure 4.3** Optical and AFM images of the coupled plasmonic nanorings.

## 4.3 The optical far-field studies of coupled plasmonic nano-assemblies by bright-field microscope and reflection dark-field microscope

Once the construction of nano assemblies was finished, the sample was viewed by the WITec Alpha 300S system under white LED illumination on reflection mode. Video was taken during gradually and slowly changing of the vertical distance (Z-value) by 20 nm for each step. The relative locations of the nano structures and their corresponding AFM

topographic images are present in figure. This sample was also viewed by reflection dark-field microscope.

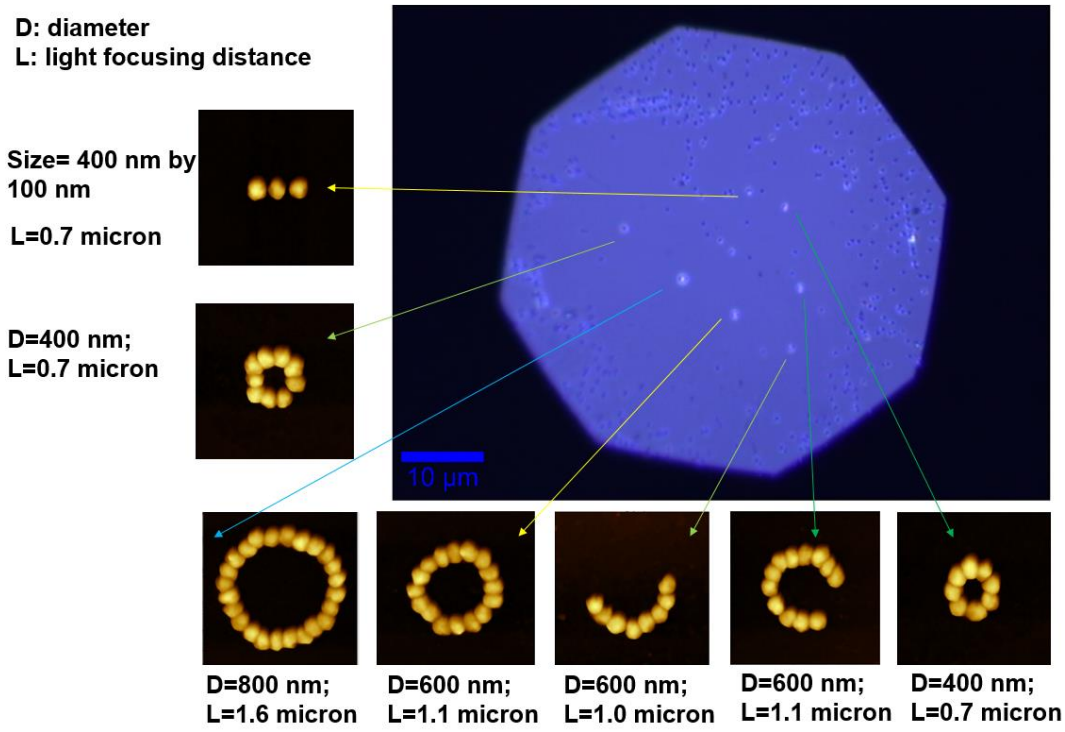


**Figure 4.4** An optical image depicting far-field focusing of light (for example by the 800 nm diameter nanoring) when viewed under white LED illumination in reflection mode. The AFM images (1 x 1 micron2) of coupled plasmonic nanorings are also shown in the figure.

### 4.3.1 The far-field observation and explanation for individual silver nanoparticles

With increasing vertical distance from the focal plane (*z* direction), a 110 nm diameter individual AgNP appears as a small shiny dot, and then its intensity gradually weakens and becomes dim. This was observed for several isolated AgNPs which happens over a $z \sim 0.4$ - 0.5 microns. It is well known that although the dimensions of an individual

AgNP are below the optical resolution limit of the dark field microscope, they can be imaged clearly with no blinking or no bleaching in an optical microscopy. The incident light in visible range drives the free conduction electrons of AgNPs into collectively oscillations, and the resultant scattered intensities are much higher than that from a non-plasmonic nanoparticle of similar size. The scattering intensity of AgNPs is considerably and useful in single molecule detection, enhanced Raman scattering, solar energy materials, and biomedical applications, etc.

As discussed in Chapter 1, the scattering cross section of a spherical particle (with radius $a$ that is smaller or comparable to the incident wavelength) is proportional $a^6$, while its absorption cross section is proportional to $a^3$ [7]. It was experimentally demonstrated (Figure 4.5) that for small AgNPs (diameter < 37 nm), adsorption dominates scattering, and hence the small AgNPs are very difficult to detect by light scattering [82]. For relatively lager AgNPs (diameter > 75 nm), scattering largely contributes to the overall extinction spectrum [82].

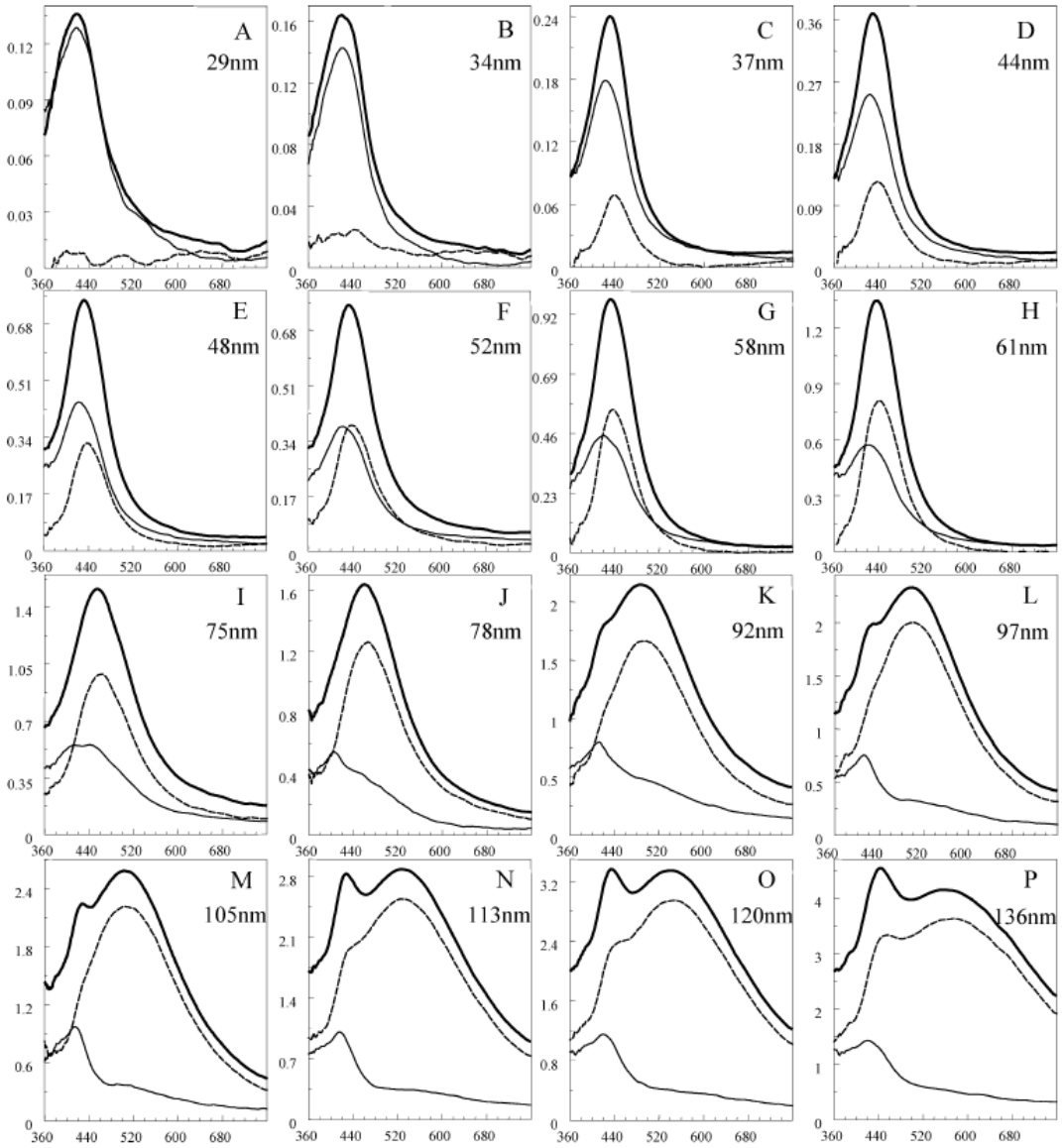


**Figure 4.5** Extinction (thick solid line), absorption (thin solid line), and scattering (dashed line) spectra of AgNP suspensions of different sizes normalized per single particle. The units on y-axis are multiplied by a factor of $10^{10}$. Figure cited from reference [82].

As isolated AgNPs were randomly located on the coverslip, and far away from each other (few microns or more), no near-field coupling is expected. Long range interactions can also be neglected since there is no long-range order among the sparsely dispersed AgNPs [83].

The scattered light by individual 110 nm AgNPs dimmed over a *z* of ~ 0.4-0.5 micron, which is understandable since the backscattered light from the 110 nm AgNPs further decreased in intensity as the scattered light dispersed and weakened in the optical far-field.

Moreover, the individual AgNPs appeared green in color when viewed under a reflection dark-field microscope (Figure 4.6) implying a scattering resonance peak around 530 nm, which is consistent with previous reports [82].

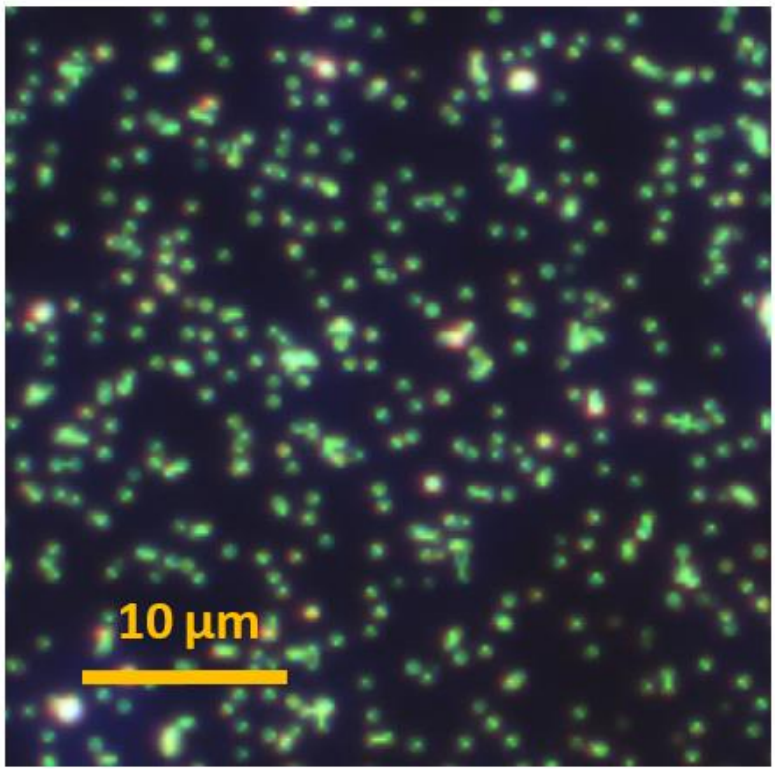


**Figure 4.6** Optical image of individual AgNPs as viewed under a reflection dark-field microscope.

### 4.3.2 The far-field focusing by a discrete AgNP trimer

The discrete AgNP trimer (100 nm x 400 nm in dimension) exhibited a remarkably high

brightness in the far field ($z$ ~ 0.7 microns) as compared to that exhibited by individual AgNPs. The AFM image of this trimer revealed three 110 nm AgNPs with an average gap of ~13 nm. It should be note that in AFM the height of AgNPs can be measure more accurately compared to their lateral dimensions, and hence the measured gap values are smaller than the true gap distances.

Discrete coupled plasmonic NPs haven drawn significant attention in recent years due to their significantly enhanced electromagnetic radiation in the gap region, which is very useful in sensing applications. Dai and co-workers proposed a delicate concept of a step-by-step electromagnetic enhancement by a cascade trimer structure made of three plasmonic nanoparticles with conspicuously different sizes (Figure 4.7) [84]. After excitation by the incident light, the biggest particle's LSPR will serve as the illumination source for the next medium sized particle wherein the electromagnetic field will be further enhanced, and subsequently the highest intensity appears between the medium-sized particle and smallest particle due to the excitation of LSPR on the smallest particle by the electromagnetic of the medium-sized particle.

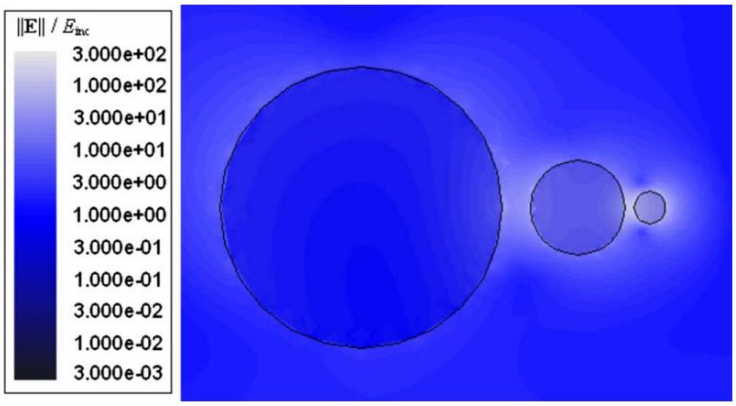


**Figure 4.7** The electric field enhancement factors exhibited by a cascade of three plasmonic spheres. Figure cited from reference [84].

Returning to the above described discrete trimer, each AgNP is only ~13 nm from its neighboring AgNP, which is much shorter than the range of LSPR for 120 nm AgNPs [20]. Thus upon excitation, the LSPRs of the three AgNPs overlap and couple with each other, leading to a much stronger light scattering.

As a further proof for the presence of plasmonic coupling in the discrete trimer, we also examined the intensity of far-field scattered light from a group of three individual 110 nm AgNPs (located to the left of the discrete trimer as seen in Figure 4.4 and Figure 4.9) with an interparticle gap distance of 350-650 nm. As expected, this group of three individual AgNPs appeared similar in intensity as other isolated AgNPs, and darker relative to the discrete trimer.

There are several reports on resonant coupling in plasmonic dimers, trimers, and chains, which are often referred as oligomers in open literature. The interparticle distance, the polarization of incident light, the configuration and shape of the oligomer all play a role in the resultant scattering resonance spectrum. When the dipoles in each individual particle are arranged in a head-to-tail orientation (longitudinal mode), charges of opposite signs accumulate on either sides of the gap, which weakens the net restoring force in the oligomer (Figure 4.8). Thus the longitudinal plasmon mode reduces the restoring force, leading to a red shift in the scattering spectrum. In contrast, in the transverse mode, the charge distribution enhances the restoring force and an increased plasmon eigenfrequency, which is equivalent to a spectral blue-shift [85]. These two bright modes contribute towards the enhanced scattering intensity. Unfortunately, due to the lack of polarizers in the dark field microscope used in this study, these bright modes could not be experimentally observed. For simplicity, the dark modes of discrete trimer are not presented and can be found [85].

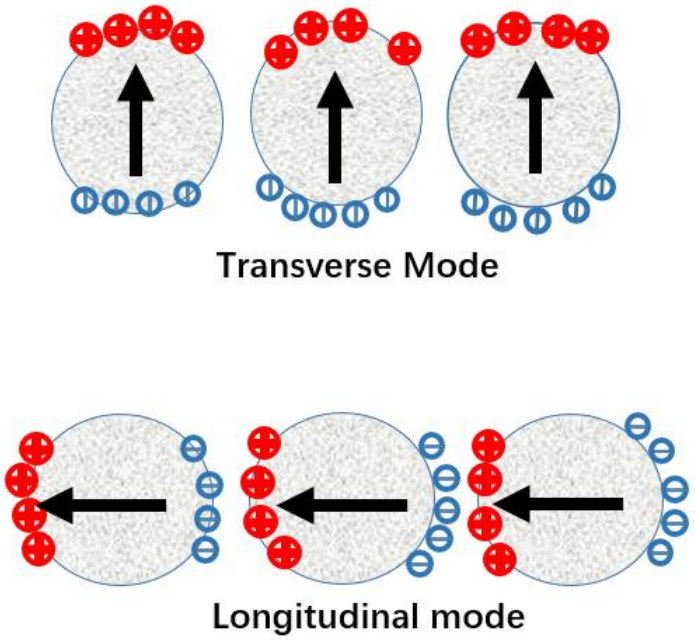


**Figure 4.8** A schematic for the two bright modes exhibited by the discrete trimer.

It is well known that the longitudinal plasmon mode has a much higher scattering cross section than the transverse plasmon mode, leading to the presence of a red-shifted peak when illuminated by unpolarized white light [85]. This theoretical prediction is consistent with our experimental observation, i.e., in reflection dark-field microscope image the group of three sparsely located AgNPs appeared green (similar to other individual AgNPs) but and the discrete trimer appeared yellow/orange in color, signaling a red-shift in its scattering spectrum.

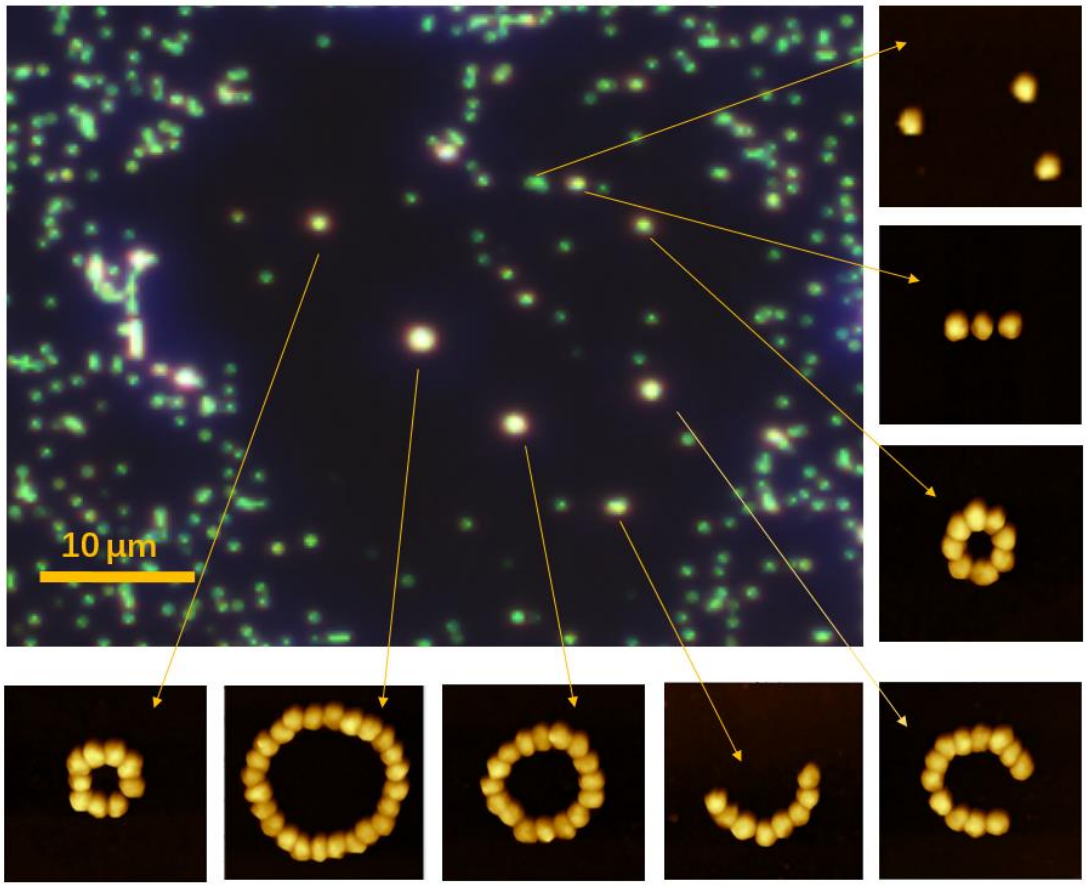


**Figure 4.9** Optical image of individual and assembled AgNPs as viewed under a reflection dark-field microscope. The corresponding AFM images (1 x 1 micron$^2$) are also shown in the figure.

### 4.3.3 The far-field focusing of nanorings

The remarkable far-field focusing of visible light by plasmonic nanorings is mainly due to the overlapping of the back scattered light. A coupled plasmonic nanoring is a wonderful design for both strong light scattering, and focusing of this scattered light in the far-field, for the following reasons:

***1)*** Silver interacts with light more strongly than any other known materials. Especially for larger AgNPs, their light scattering ability increases with increasing diameter because more free conduction electrons are present in the larger AgNP resulting in a larger scattering cross section. For the nanorings discussed in this chapter, individual AgNPs were placed in such a way that they are in close contact with neighboring AgNPs, and the conduction electrons of each AgNP becomes part of the electron cloud which is spread across the entire ring structure. Thus, compared with individual silver nanoparticle, the nanorings have more free conduction electrons and hence much larger scattering cross section.

***2)*** The single crystalline AgNPs used in this study were prepared using wet chemistry methods. The AgNPs contain very limited numbers of internal boundaries, which means less radiation energy will be wasted in the form of heat.

***3)*** Compared with an ideally smooth ring, the constructed nanorings have a wavy terrain (on the scale of nanometers, but not that high enough to affect the height uniformity and homogeneity of the nanorings), and sometimes sharp corners of single crystalline polygonal AgNPs. Such roughness contributes supports strong light scattering because radiation tends to emit at a rougher surface.

***4)*** The plasmonic mode of individual AgNPs are coupled in a nanoring, leading to a highly coupled plasmon resonance. The AgNPs within the nanoring contact each other and can thus the nanoring can be viewed as a large plasmonic molecule, which is consistent with the observed red-shift in the forward scattering resonance spectrum measured by the transmission dark-field microscope.

5) It is reasonable to expect the nanoring to behave as a focusing lens under certain experimental conditions. Such behavior has been observed in this study, for example, the far field focusing of light by the 24-particle nanoring; however, a rigorous explanation is presently lacking.

### 4.3.4 The 24-particle-nanoring

As described previously in Figure 4.3, the 24-particle nanoring has an outer diameter of ~800 nm and an inner diameter of ~600 nm. The 24-particle-nanoring appeared as a white bright ring (with an outer diameter of 1200 nm and an inner diameter of 350 nm) at the focal plane, which corresponded to a $z$ = 0 microns. The image of this ring could be discerned even up to $|z| \sim 0.7$ microns, beyond which it became fuzzy as well as expanded in size. Interestingly, the central spot which was previously dark became brighter and brighter until a bright spot (420 - 500 nm in diameter) appeared in the image at $z$ = 0.91-1.63 micron. The intensity profiles are depicted Figure 4.10.

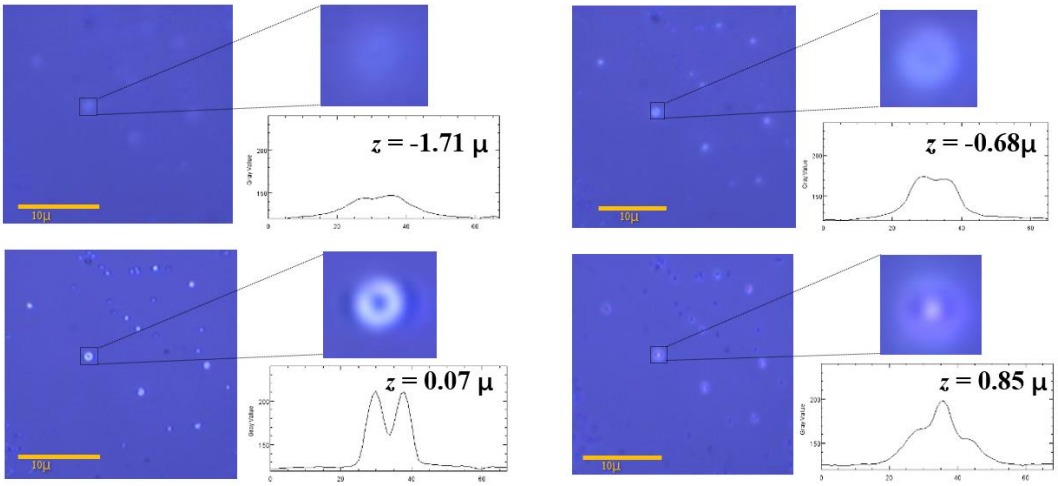


**Figure 4.10** The optical images of the 24- particle plasmonic nanoring at varying z positions. The inserts represent zoomed-in views of the optical images and intensity profiles.

Figure 4.11 depicts the Mie scattering lobes that are expected for polarized or unpolarized light scattered by an AgNP. The strongly coupled plasmonic modes in the nanoring is expected to influence the shape of the backscattered Mie lobe, for example, higher order plasmonic modes may result in multiple backscattered Mie lobes. However, for simplicity,

we represent the backscattered Mie lobes as shown in Figure 4.12.

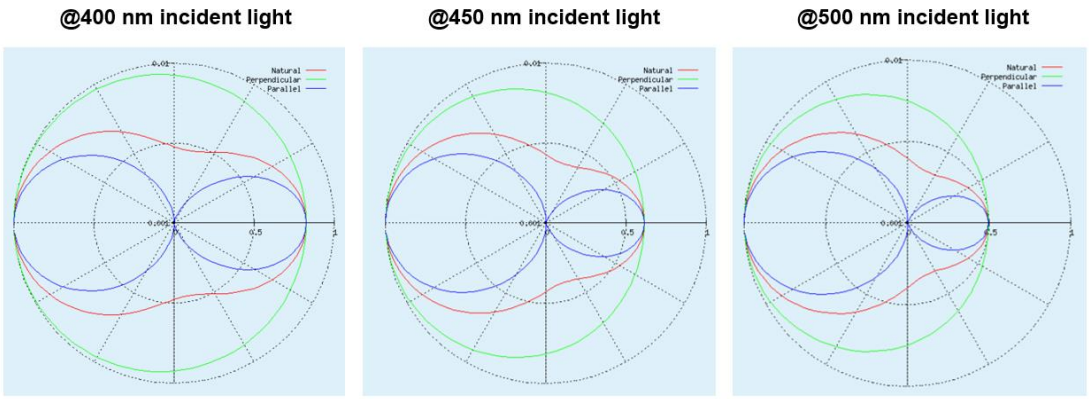


**Figure 4.11** Mie scattering plots for a 110 nm AgNP. Unpolarized (red), perpendicular polarized (green) or parallel polarized (blue) light is incident from the left hand side of the spherical AgNP located at the center of the polar plot.

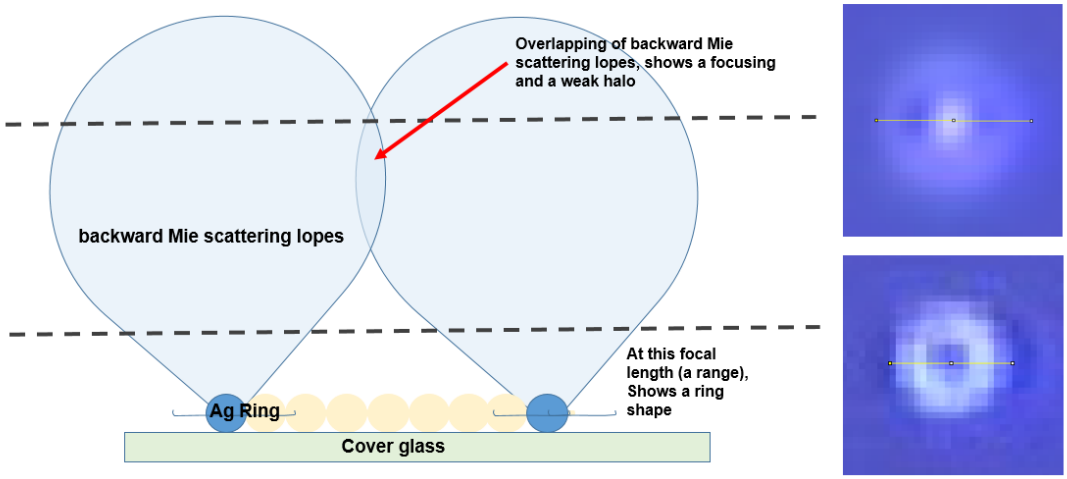


**Figure 4.12** A plausible mechanism for far field focusing of light by a nanoring due to its overlapping backscattered Mie lobes.

### 4.3.5 The 16-particle-nano-ring

A 16-particle nanoring showed a similar light focusing behavior as the 24-particle nanoring, but with a relatively shorter light focusing distance range ( $z$ = 0.97-1.25 micron). This behavior can be explained in terms of overlapping backscattered Mie lobes as depicted in Figure 4.12. As the ring diameter decreases, the far field light focusing distance decreases as well since the backscattered Mie scattering lobes overlap at a smaller $z$ value.

### 4.3.6 The 8, 9-particle-nano-rings

The 8 and 9-particle nanorings also exhibited far field light focusing. Consistent with the reduced focusing distance exhibited by the 16-particle nanoring, the 8 and 9-particle nanorings exhibited an even smaller focusing distance of ~0.7 micron. However, the images for the far field focusing by the 8 and 9-particle nanorings are not as crisp as the images cast by the 24-particle nanoring. The far field light focusing distance as a function of the nanoring diameter is depicted in Figure 4.13, which approximately mimics the dependence reported for a micro-lens.

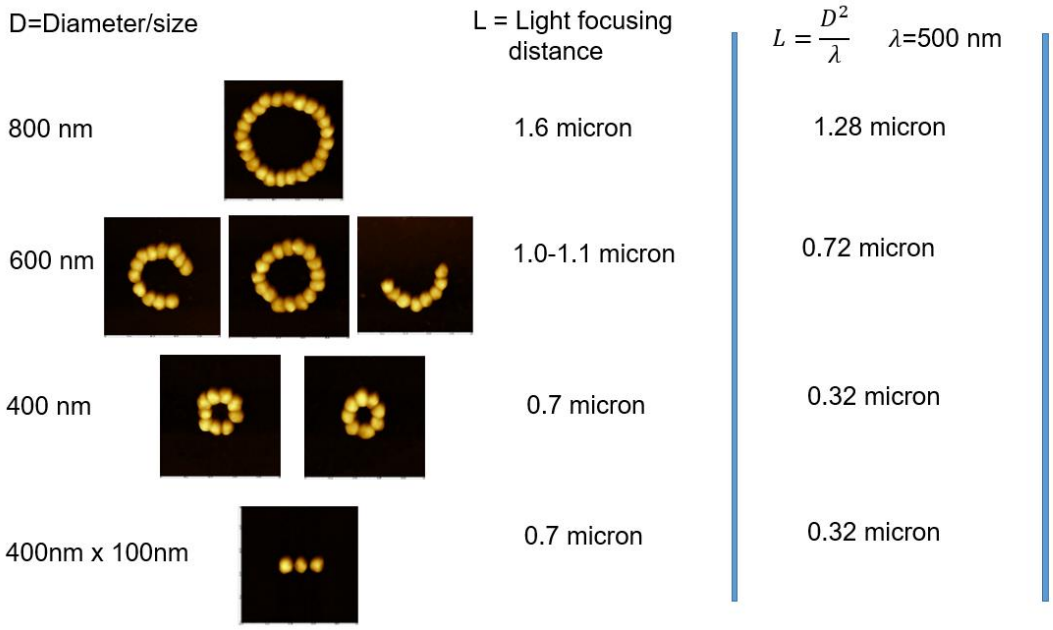

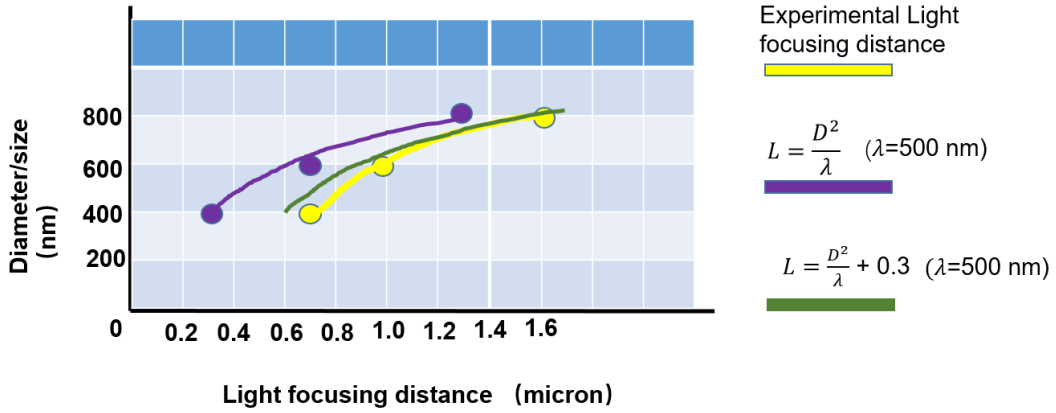


**Figure 4.13** Comparison of experimentally determined light focusing distance *L* (yellow) for nanorings used in this study to empirically derived *L* (purple) for a micro-lens [86]. While similar trends are observed for the yellow and purples traces in the above figure, a better agreement is achieved when the purple trace is upshifted by 0.3 microns.

### 4.3.7 The far field focusing behavior of incomplete nanorings

As shown in Figure 4.4 above, two incomplete nanorings were also assembled in this study: 1) a 12 particle crescent which can be considered as a three-fourth section of a 16-particle nanoring; and 2) an 8 particle crescent which can be considered as half of the 16-particle nanoring. As seen in their corresponding AFM images, both crescents have the same diameter (~600 nm) as the 16-particle nanoring. The 8- and 12-particle crescents show similar light focusing behavior as the 16-particle nanoring, albeit the intensities are weaker for 8-particle nanoring. However, almost similar light focusing distances were measured for the 8- and 12-particles crescents, which was similar to that of 16-particle nanoring.

## 4.4 Dark-field transmission spectral fingerprints of coupled plasmonic nanorings

### 4.4.1 Influence of the shape of plasmonic assemblies on the scattering spectrum

To better understand how the shape of plasmonic assemblies influence the s scattering resonance spectrum, we prepared three oligomers each comprised of 8 AgNPs as follows: 1) an 8-particle nanoring; 2) an 8-particle crescent: and 3) an 8-particle linear chain. Their scattering resonance spectra were measured using a transmission dark-field microscope, and presented in Figure 4.14. The 8-particle nanoring and the 8-particle crescent have diameters of ~400 and ~600 nm, respectively, while the linear chain is 1000 nm in length. Figure 4.15 shows the possible charge density distributions of various LSPR modes for these assemblies, which lead to the observed differences in the scattering spectrum depicted in Figure 4.14.

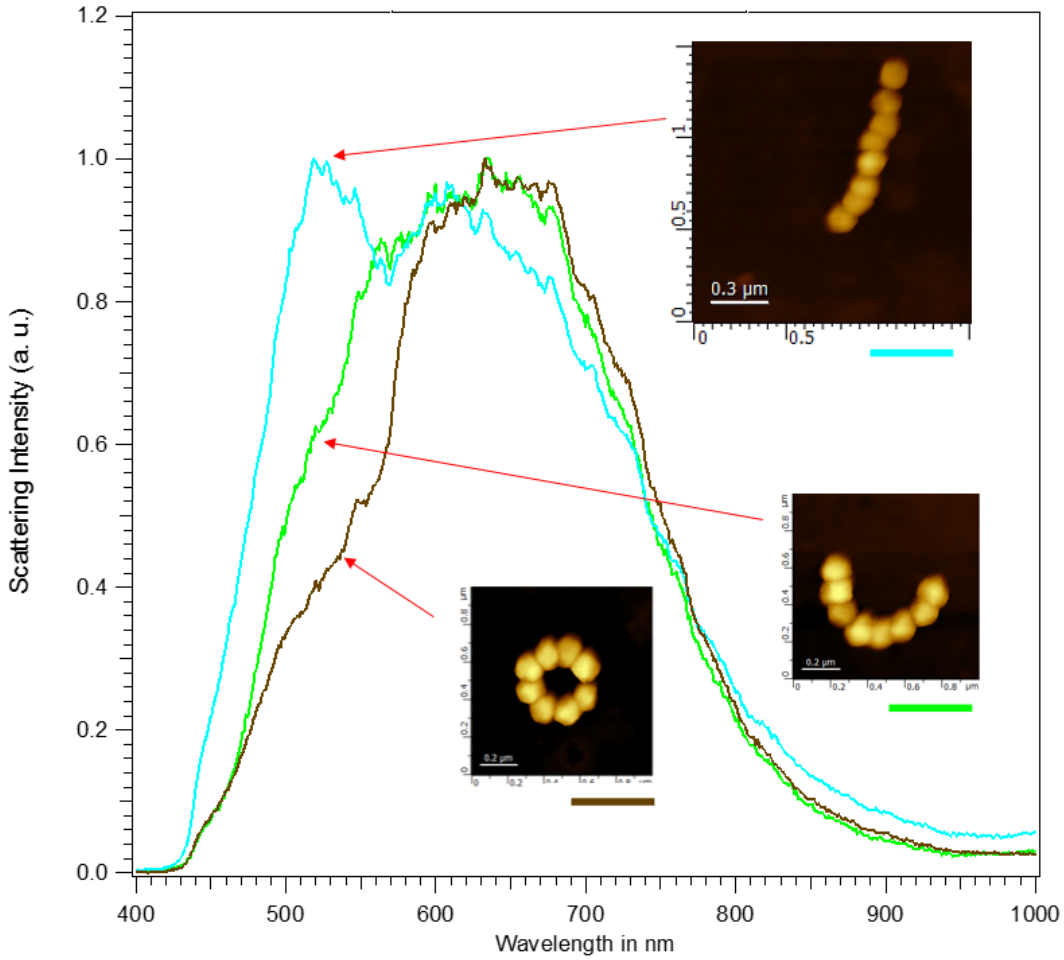


**Figure 4.14** The AFM images of 8-particle nanoring, 8-particle crescent and 8-particle linear chain, and their scattering resonance spectra measured by transmission dark-field microscope.

The 8-particle linear chain shows two distinct peaks in Figure 4.14, which are due to the red (blue) shift caused by the longitudinal (transverse) modes explained in Figure 4.8. The relatively weaker transverse mode appears strong in this case due to the number of AgNPs present in the chain.

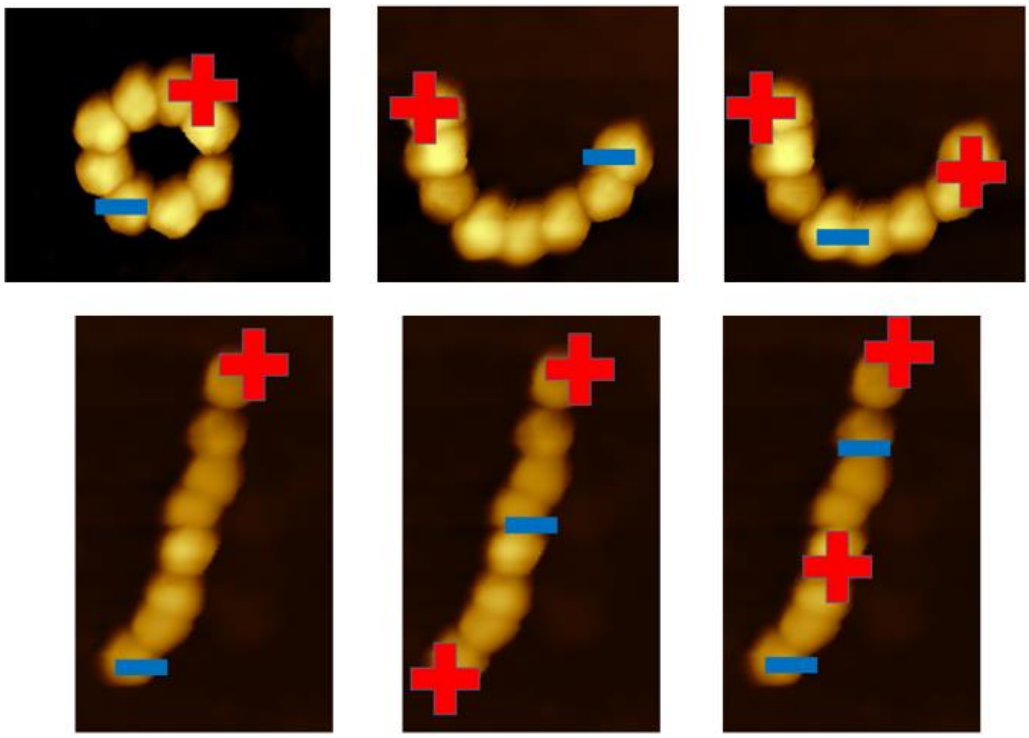

**Figure 4.15** The possible charge density distributions of various LSPR modes for the 8-particle nanoring, 8-particle crescent, and a 8-particle linear chain.

The transmission dark-field microscope images of plasmonic nanorings and their scattering resonance spectra are presented in Figure 4.16. The electromagnetic field is relatively more uniform for the smaller 8-particle nanorings, and the major peak in its scattering spectrum appears in the red. As the size of the nanoring increases, higher order modes appear in the blue spectral region. For simplicity, if we only consider dipoles, the transvers mode intensity increases as the size of the nanorings increase, leading to a more intense peak in the blue spectral region.

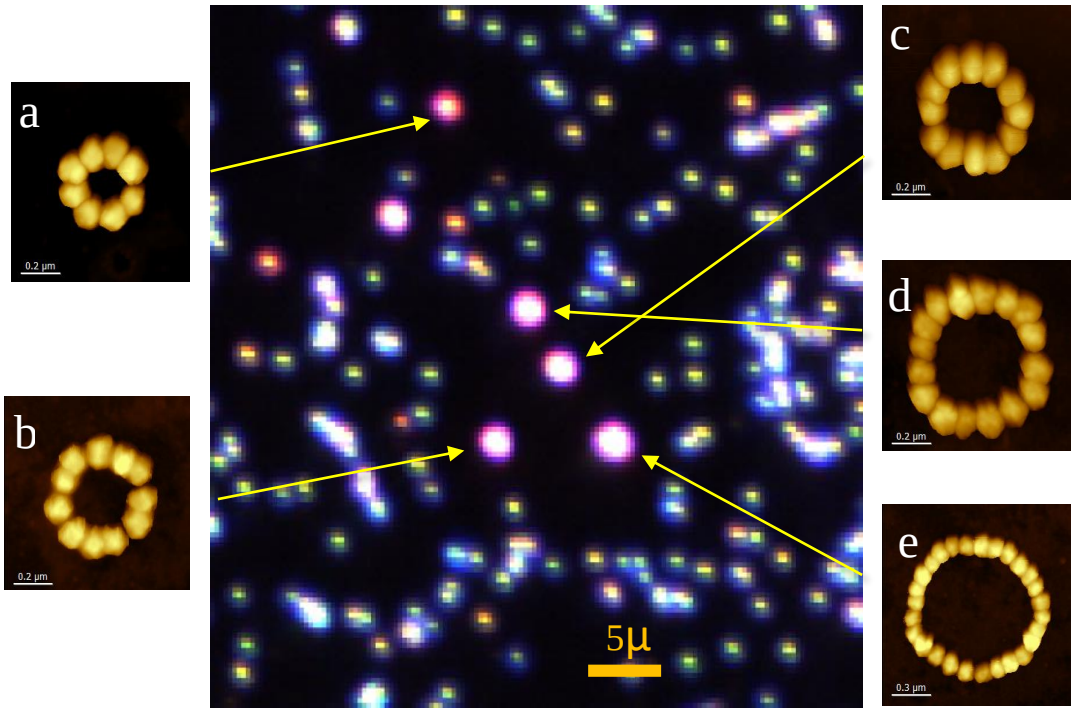


**Figure 4.16** Dark-field transmission microscope image of plasmonic nanorings. The associated AFM images for each of the nanorings consisting of 8, 11, 12, 16 and 27 AgNPs as marked (a), (b), (c), (d) and (e), respectively.

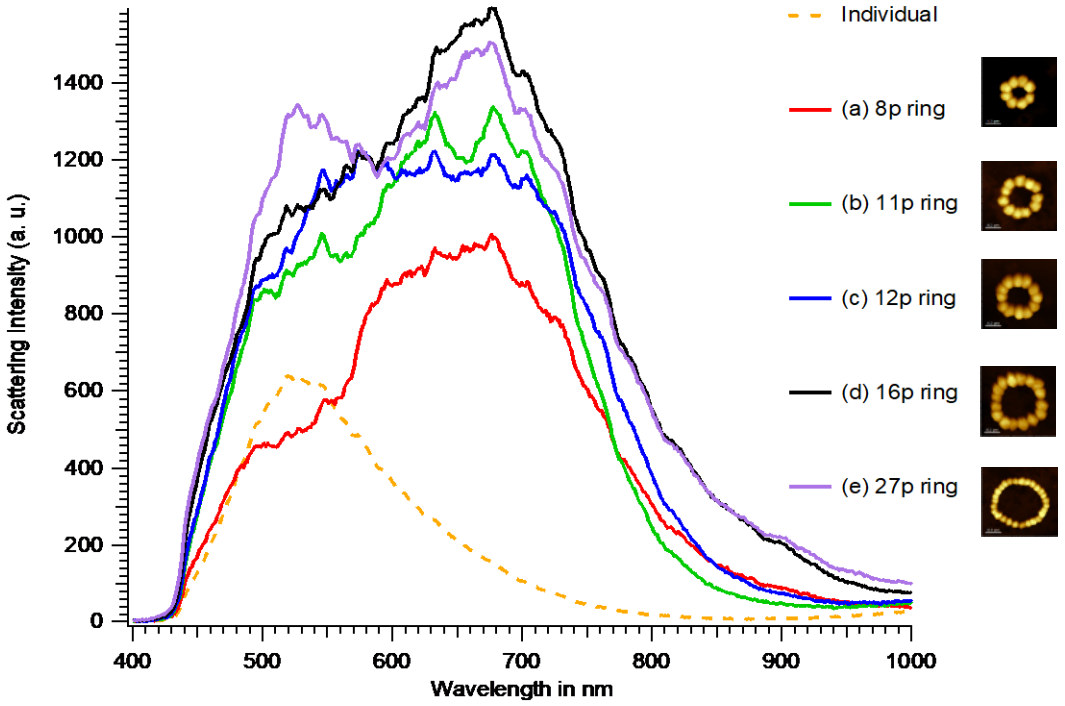


**Figure 4.17** The scattering spectra of 8, 11, 12, 16, and 27 particle nanorings compared to that of an individual AgNP.

In conclusion, discrete trimer, silver nano-ring structures of various diameters, and uncompleted rings were constructed by AFM manipulation and far-field light focusing was achieved under reflection illumination which has great application in manipulation of light in nano-optics and bio-sensoring.

# Bibliography


[1]. S. Sugumaran, M.F. Jamlos and M.N. Ahmad. Nanostructured materials with plasmonic nanobi osensors for early cancer detection: A past and future prospect. *Biosensors & Bioelectronics*, 2 017. 100: p. 361.

[2]. P. Mandal and S. Sharma. Progress in plasmonic solar cell efficiency improvement: A status review. *Renewable & Sustainable Energy Reviews*, 2016. 65: p. 537-552.

[3]. S. Khatua. Resonant Plasmonic Enhancement of Single-Molecule Fluorescence by Individual Gold Nanorods. *Acs Nano*, 2014. 8(5): p. 4440-9.

[4]. W. Li. Plasmonic substrates for surface enhanced Raman scattering. *Analytica Chimica Acta*, 2017. 984: p. 19.

[5]. A.V. Arsenin. D.A. Svintsov and D.Y. Fedyanin, Full loss compensation in hybrid plasmonic waveguides under electrical pumping. *Optics Express*, 2015. 23(15): p. 19358-75.

[6]. T.P. Wallace. The scattering of light and other electromagnetic radiation by Milton Kerker. Academic Press, *Journal of Polymer Science Part A-2 Polymer Physics*, 1970. 8(5): p. 813-813.

[7]. X. W. Fan, Zheng and D.J. Singh. Light scattering and surface plasmons on small spherical particles. *Light Science & Applications*, 2014. 3(6): p. e179.

[8]. X.C. Ma. Energy transfer in plasmonic photocatalytic composites. *Light Science & Applications*, 2016. 5(2): p. e16017.

[9]. M.K. Zahran, H.B. Ahmed and M.H. Elrafie. Surface modification of cotton fabrics for antibacterial application by coating with AgNPs-alginate composite. *Carbohydrate Polymers*, 2014. 108(108): p. 145-152.

[10]. K. Rajan. Silver nanoparticle ink technology: state of the art. *Nanotechnology Science & Applications*, 2016. 9: p. 1-13.

[11]. B. Martin. Plasmon-Enhanced Fluorescence Biosensors: a Review. *Plasmonics*, 2014. 9(4): p. 781-799.

[12]. D.K. Rechenberg, J.C. Galicia and O.A. Peters. Biological Markers for Pulpal Inflammation: A Systematic Review. *Plos One*, 2016. 11(11): p. e0167289.

[13]. M. Li, S.K. Cushing and N. Wu. Plasmon-Enhanced Optical Sensors: A Review. *Analyst*, 2015. 140(2): p. 386-406.

[14]. C. Caucheteur. Ultrasensitive plasmonic sensing in air using optical fibre spectral combs. *Nature Communications*, 2016. 7: p. 13371.

[15]. D.D Evanoff and G. Chumanov. Size-Controlled Synthesis of Nanoparticles. 1.Silver-Only? Aqueous Suspensions via Hydrogen Reduction. *Journal of Physical Chemistry B*, 2004. 108(37).

[16]. Y.H. Fu. Directional visible light scattering by silicon nanoparticles. *Nature Communications*, 2012. 4(2): p. 1527.

[17]. J.K. Daniels and G. Chumanov. Nanoparticle mirror Sandwich Substrates for Surface-Enhanced Raman Scattering. *Journal of Physical Chemistry B*, 2005. 109(38): 17936-42.

[18]. S.D. Hudson and G. Chumanov. Bioanalytical applications of SERS (surface-enhanced Raman spectroscopy). *Analytical & Bioanalytical Chemistry*, 2009. 394(3): p. 679.

[19]. Z.Z. Yao and Z. Guang. Stable and Uniform SERS Signals from Self-Assembled Two-Dimensional Interfacial Arrays of Optically Coupled Ag Nanoparticles. *Analytical Chemistry*, 2013. 85(14): p. 6783-9.

[20]. M.K. Kinnan and G. Chumanov. Plasmon Coupling in Two-Dimensional Arrays of Silver Nanoparticles: II. Effect of the Particle Size and Interparticle Distance, *Journal of Physical Chemistry C*, 2010. 114(16): 7496-7501.

[21]. M.K. Kinnan. Plasmon Coupling in Two-Dimensional Arrays of Silver Nanoparticles: I. Effect of the Dielectric Medium. *Journal of Physical Chemistry C*, 2009. 113(17): p. 7079-7084.

[22]. S. Malynych, A. Holly Robuck and G. Chumanov. Fabrication of Two-Dimensional Assemblies of Ag Nanoparticles and Nanocavities in Poly(dimethylsiloxane) Resin. *Nano Letters*, 2001. 1(11): p. 647-649.

[23]. S.J. Barcelo. Nanosphere lithography based technique for fabrication of large area well ordered metal

particle arrays. *Advanced Lithography*, 2012. 8323: p. 60.

[24]. D.L. John. DNA-Templated Self-Assembly of Metallic Nanocomponent Arrays on a Surface. *Nano Letters*, 2004. 4(12): p. 2343-2347.

[25]. J. Zheng. Two-dimensional Nanoparticle Arrays Show the Organizational Power of Robust DNA Motifs. *Nano Letters*, 2006. 6(7): p. 1502-4.

[26]. H. Mizuno. Capturing by self-assembled block copolymer thin films: transfer printing of metal nanostructures on textured surfaces. *Chemical Communications*, 2013. 50(3): p. 362-4.

[27]. Q. Xia and S.Y. Chou. The fabrication of periodic metal nano dot arrays through pulsed laser melting induced fragmentation of metal nanogratings. *Nanotechnology*, 2009. 20(28): p. 285310.

[28]. A.I. Kuznetsov, R. Kiyan and B.N. Chichkov. Laser fabrication of 2D and 3D metal nanoparticle structures and arrays. *Optics Express*, 2010. 18(20): p. 21198-21203.

[29]. R.A. Sperling and W.J. Parak. Surface modification, functionalization and bioconjugation of colloidal inorganic nanoparticles. *Philosophical Transactions Mathematical Physical & Engineering Sciences*, 2010. 368(1915): p. 1333.

[30]. T. Yonezawa and T. Kunitake. Practical preparation of anionic mercapto ligand-stabilized gold nanoparticles and their immobilization. *Colloids & Surfaces A Physicochemical & Engineering Aspects*, 1999. 149: p. 193-199.

[31]. M. Brust and M. Walker. Self-Assembled Monolayers of Thiolates on Metals as a Form of Nanotechnology. *Chemical Reviews*, 2005. 105(4): p. 1103-69.

[32]. M.M. Brust. Synthesis of Thiol-Derivatized Gold Nanoparticles in a 2-Phase Liquid-Liquid System. *Journal of the Chemical Society Chemical Communications*, 1994. 7(7): p. 801-802.

[33]. W. Cheng, S. Dong and E. Wang. Iodine-induced gold-nanoparticle fusion/fragmentation/aggreg ation and iodine-linked nanostructured assemblies on a glass substrate. *Angewandte Chemie*, 20 03. 42(4): p. 449.

[34]. M.C. Daniel and D. Astruc. Gold Nanoparticles: Assembly, Supramolecular Chemistry, Quantum-size-

related Properties, and Applications Toward Biology, Catalysis, and Nanotechnology. *Chemical Reviews*, 2004. 104(1): 293.

[35]. H.S. Kim. Adsorption Characteristics of 1,4-Phenylene Diisocyanide on Gold Nanoparticles: Infrared and Raman Spectroscopy Study. *Langmuir*, 2003. 19(17): 6701-6710.

[36]. D.V. Leff, L. Brandt and J.R. Heath. Synthesis and Characterization of Hydrophobic, Organically-Soluble Gold Nanocrystals Functionalized with Primary Amines. *Langmuir*, 1996. 12(20): p. 4723-4730.

[37]. G.T. Li. Spherical and Planar Gold(0) Nanoparticles with a Rigid Gold(I)-Anion or a Fluid Gold(0) Acetone Surface. *Langmuir*, 2003. 19(16): 6483-6491.

[38]. P. Selvakannan e. Capping of Gold Nanoparticles by the Amino Acid Lysine Renders Them Water-Dispersible. *Langmuir*, 2003. 19(19): p. 3545.

[39]. W.W.Weare. Improved Synthesis of Small (dCORE approximate to 1.5 nm) Phosphine-Stabilized Gold Nanoparticles. *Journal of the American Chemical Society*, 2000. 122(51).

[40]. M. Yamamoto and M. Nakamoto. New Type of Monodispersed Gold Nanoparticles Capped by Myristate and PPh3 Ligands Prepared by Controlled Thermolysis of [Au(C13H27COO)(PPh3)]. *Chemistry Letters*, 2003. 32(5): p. 452-453.

[41]. T. Sakura, T. Takahashi, K. Kataoka, Y. Nagasaki, One-pot preparation of mono-dispersed and physiologically stabilized gold colloid. *Colloid Polymer Science*, 284 (2005) 97–101.

[42]. M. Tejamaya, I. Roemer, R.C. Merrifield, J.R. Lead, Stability of citrate, PVP, and PEG coated silver nanoparticles in ecotoxicology media. *Environmental Science and technology*, 46 (2012) 7011–7017.

[43]. B. Ballou, B.C. Lagerholm, L.A. Ernst, M.P. Bruchez, A.S. Waggoner, Noninvasive imaging of quantum dots in mice. *Bioconjugate Chemistry*, 15 (2004) 79–86.

[44]. T.J. Daou, L. Li, P. Reiss, V. Josserand, I. Texier, Effect of poly(ethylene glycol)length on the in vivo behavior of coated quantum dots, *Langmuir*.25 (2009)3040–3044.

[45]. R. Gref, M. Luck, P. Quellec, M. Marchand, E. Dellacherie, S. Harnisch, T. Blunk,R.H. Muller,‘Stealth’ corona-core nanoparticles surface modified by polyethylene glycol (PEG): influences

of the corona (PEG chain length and surface density) and of the core composition on phagocytic uptake and plasma protein adsorption. *Colloids and Surfaces B: Biointerfaces*, 18 (2000) 301–313.

[46]. K. Esumi, N. Takei, T. Yoshimura, Antioxidant-potentiality of gold-chitosannanocomposites, *Colloids and Surfaces B: Biointerfaces*, 32 (2003) 117–123.

[47]. H.Z. Huang, X.R. Yang, Synthesis of chitosan-stabilized gold nanoparticles in the absence/presence of tripolyphosphate. *Biomacromolecules*, 5 (2004)2340–2346.

[48]. G. Fritz, V. Schadler, N. Willenbacher, N.J. Wagner, Electro steric stabilization of colloidal dispersions. *Langmuir*, 18 (2002) 6381–6390.

[49] Y.A. Wang, J.J. Li, H.Y. Chen, X.G. Peng, Stabilization of inorganic nanocrystals by organic dendrons. *Journal of the American Chemical Society*, 124 (2002) 2293–2298.

[50] J. Zheng, M.S. Stevenson, R.S. Hikida, P.G. Van Patten, Influence of pH on dendrimer-protected nanoparticles. *Journal of Physical Chemistry A*, B 106 (2002) 1252–1255.

[51]. K. Chen, C.-C. Lin, J. Vela, N. Fang, Multi shell Au/Ag/SiO2nanorods with tunable optical properties as single particle orientation and rotational tracking probes. *Analytical Chemistry*, 87 (2015) 4096–4099.

[52]. S. Raj, P. Rai, S.M. Majhi, Y.-T. Yu, Morphology controlled Ag@SiO2core–shell nanoparticles by ascorbic acid reduction. *Journal of Materials Science: Materials in Medicine*, 25(2014) 1156–1161.

[53]. W. Stober, A. Fink, E. Bohn, Controlled growth of monodisperse silica spheresin the micron size range. *Journal of Colloid and Interface Science*, 26 (1968) 62–69.

[54]. N.M. Khaa, C.-H. Chen, W.-N. Sub, J. Rickb, B.-J. Hwang, Improved Raman and photoluminescence sensitivity achieved using bifunctional Ag@SiO2nanocubes. *Physical Chemistry Chemical Physics*, (2015).

[55]. Y. Chaikin, O. Kedem, J. Raz, A. Vaskevich, I. Rubinstein, Stabilization of metalnanoparticle films on glass surfaces using ultrathin silica coating. *Analytical Chemistry*, 85 (2013) 10022–10027.

[56]. M. Kanungo, P.N. Deepa, M.M. Collinson, Template-directed formation of hemispherical cavities of

varying depth and diameter in a silicate matrix prepared by the sol-gel process. *Chemistry of Materials*, 16 (2004) 5535–5541.

[57] A.N. Khramov, J. Munos, M.M. Collinson, Preparation and characterization of macroporous silicate films. *Langmuir*, 17 (2001) 8112–8117.

[58]. S. Malynych, I. Luzinov, G. Chumanov, Poly(vinyl pyridine) as a universalsurface modifier for immobilization of nanoparticles. *Journal of Physical Chemistry B*, 106(2002) 1280–1285.

[59]. Y.N. Xia, E. Kim, G.M. Whitesides, Microcontact printing of alkanethiols on silver and its application in microfabrication. *Journal of the Electrochemical Society*, 143 (1996)1070–1079.

[60]. A.L. Pfirman, The Fabrication and Study of Silver Nanoparticle Structures, Chemistry, Clemson University, 2013.

[61]. G.B. Gonzalez, Investigating the defect structures in transparent conducting oxides using X-ray and neutron scattering techniques. *Materials,* 5 (2012)818–850.

[62]. K. P. Carter, A. M. Young, and A. E. Palmer, Fluorescent Sensors for Measuring Metal Ions in Living Systems. *Chemical Reviews,* 114, no. 8 (2014): 4564–4601.

[63]. S.Kruss, A. J. Hilmer, J. Zhang, N. F. Reuel, B. Mu, and M. S. Strano, Carbon Nanotubes as Optical Biomedical Sensors. *Advanced Drug Delivery Reviews*, 65, no. 15 (2013): 1933–1950.

[64]. M. Sauer, Single-Molecule-Sensitive Fluorescent Sensors Based on Photoinduced Intramolecular Charge Transfer. *Angewandte Chemie - International Edition*, 42, no. 16 (2003).

[65]. E. Zamir, P. H. M. Lommerse, A. Kinkhabwala, H. E. Grecco, and P. I. H. Bastiaens, Fluorescence Fluctuations of Quantum-Dot Sensors Capture Intracellular Protein Interaction Dynamics. *Nature Methods 7*, no. 4 (2010): 295–298.

[66]. G. Orellana, FLUORESCENCE-BASED SENSORS. *Optical Chemical Sensors* 224, (2006): 99–116.

[67]. J. C. Pickup, F. Hussain, N. D. Evans, O. J. Rolinski, and D. J. S. Birch, Fluorescence-Based Glucose Sensors. *Biosensors and Bioelectronics* 20, no. 12 (2005): 2555–2565.

[68]. M. E. Stewart, C. R. Anderton, L. B. Thompson, J. Maria, S. K. Gray, J. A. Rogers, and R. G. Nuzzo, Nanostructured Plasmonic Sensors. *Chemical Reviews*, 108, no. 2 (2008): 494–521.

[69]. R.Thompson, Fluorescence Sensors and Biosensors. *Fluorescence sensors and biosensors*, (2005).

[70]. B. Valeur, and M. N. Berberan-Santos, Chemical Sensing via Fluorescence. *Molecular Fluorescence*, no. 2011 (2012): 409–478.

[71]. O. S. Wolfbeis, Materials for Fluorescence-Based Optical Chemical Sensors. *Journal of Materials Chemistry*, 15, no. 27-28 (2005): 2657.

[72]. Y. Fu, J. Zhang, and J. R. Lakowicz, Plasmonic Enhancement of Single-Molecule Fluorescence near a Silver Nanoparticle. *Journal of Fluorescence*, 17, no. 6 (2007): 811–816.

[73]. H. Mertens, A. F. Koenderink, and A. Polman, Plasmon-Enhanced Luminescence near Noble-Metal Nanospheres: Comparison of Exact Theory and an Improved Gersten and Nitzan Model. *Physical Review B - Condensed Matter and Materials Physics*. 76, no. 11 (2007).

[74]. P. Mulpur, S. Yadavilli, A. M. Rao, R. Podila, and V. Kamisetti, MoS2/WS2/BN-Silver Thin-Film Hybrid Architectures Displaying Enhanced Fluorescence via Surface Plasmon Coupled Emission for Sensing Applications. *ACS Sensors* (2016): acssensors.5b00297.

[75]. S.-H. Cao, W.-P. Cai, Q. Liu, and Y.-Q. Li, Surface Plasmon–Coupled Emission: What Can Directional Fluorescence Bring to the Analytical Sciences? *Annual Review of Analytical Chemistry* 5, no. 1 (2012): 317–336.

[76]. I. Gryczynski, J. Malicka, Z. Gryczynski, and J. R. Lakowicz, Surface Plasmon-Coupled Emission with Gold Films. *Journal of Physical Chemistry B*, 108, no. 33 (2004): 12568–12574.

[77]. P. Anger, P. Bharadwaj, and L. Novotny, Enhancement and Quenching of Single-Molecule Fluorescence. *Physical Review Letters*, 96, no. 11 (2006).

[78]. D. D. Evanoff, and G. Chumanov, Size-Controlled Synthesis of Nanoparticles. 2. Measurement of Extinction, Scattering, and Absorption Cross Sections. *The Journal of Physical Chemistry B* 108, no. 37 (2004): 13957–13962.

[79]. P. B. Johnson, and R. W. Christy, Optical Constants of the Noble Metals. *Physical Review B* 6, no. 12 (1972): 4370–4379.

[80]. Y. S. Kim, P. T. Leung, and T. F. George, Classical Decay Rates for Molecules in the Presence of a Spherical Surface: A Complete Treatment. *Surface Science* 195, no. 1-2 (1988): 1–14.

[81]. H. Chew, Transition Rates of Atoms near Spherical Surfaces. *The Journal of Chemical Physics* 87, no. 2 (1987): 1355–1360.

[82]. D.D. Evanoff and G. Chumanov. Size-controlled synthesis of nanoparticles. 2. Measurement of extinction, scattering, and absorption cross sections. *The Journal of Physical Chemistry B* 108.37 (2004): 13957-13962.

[83]. B. Lamprecht, G. Schider, R.T. Lechner, H. Ditlbacher. Metal nanoparticle gratings: influence of dipolar particle interaction on the plasmon resonance. *Physical review letters*, 84(20), 4721.

[84]. J.H. Dai, C. Frantisek, T. Igor, and I.S. Mark. Electrodynamic effects in plasmonic nanolenses. *Physical Review B* 77, no. 11 (2008): 115419.

[85]. A.M. Funston, J.D. Timothy, N. Carolina, and M. Paul. Coupling modes of gold trimer superstructures. *Mathematical, Physical and Engineering Sciences* 369, no. 1950 (2011): 3472-3482.

[86]. P. Ruffieux, S. Toralf, P.H. Herzig, V. Reinhard, and J.W.Kenneth. On the chromatic aberration of microlenses. *Optics express* 14, no. 11 (2006): 4687-4694.

[87]. S. A. Fathima, V. Shilpa, W. B Donald, etc. and N. A. Jeffrey. Tuning Localized Surface Plasmon Resonance Wavelengths of Silver Nanoparticles by Mechanical Deformation. *The Journal of Physical Chemistry C* 120 (2016): 20886−20895